Stationary versus Bifurcation regime for Standing Wave Central Pattern Generator[☆]

R. Martin-del-Campo[a,*], E. Jonckheere[a]

[a] *Electrical Engineering Dept., University of Southern California, Los Angeles, CA 90089-2563, United States*

Abstract

The purpose of this research is to show that the correlation analysis on surface Electromyographic (sEMG) signals that originally confirmed existence of a standing wave Central Pattern Generator (CPG) along the spine are reproducible despite evolution of the entrainment technique, different hardware and data collection protocol. Moreover, as major novelty of the research, it is shown that this CPG can undergo "bifurcation," here interpreted in a signal processing sense. The visually intuitive manifestation of the bifurcation is statistically confirmed—using bootstrap analysis—by showing that the standing wave occurs on different subbands of the Daubechies DB3 wavelet decomposition of the sEMG signals.

Keywords: Central Pattern Generator; Surface Electromyography; Bifurcation; Coherence; Wavelets; Bootstrapping

1. Introduction

1.1. Background

The so-called *spinal wave* [1] is a visually obvious phenomenon during which the spine goes through a rhythmic [2] oscillation elicited by light finger pres-

[☆] Research approved by the Institutional Review Board (IRB) of the University of Southern California and supported by the Global Gateway Foundation.

[*] Corresponding author at: 3819 Flower Dr., Apt 7, Los Angeles, CA 90037-1320, United States. Tel.: +1 213 290 2315.

Email addresses: mart737@usc.edu (R. Martin-del-Campo), jonckhee@usc.edu (E. Jonckheere)

URL: http://eudoxus2.usc.edu (E. Jonckheere)

sure at some sensitized areas of the spine, typically, the neck and the sacrum. As argued in our original work [1], Alf Breig's dural-vertebral attachments [3] close sensory-motor loops in both the neck and the sacrum, creating localized oscillations, which soon propagate along the spine to settle in a standing wave pattern. The crucial features that the movement is rhythmic, that after some initial stimulus it becomes self-sustained and hence has no sensory input, already point to a Central Pattern Generator (CPG), a concept that is still an active area of research [4]. Moreover, as reported in the earlier paper [1], a quadriplegic subject with a C2-C3 injury was able to experience some spinal wave pattern, which indicates that the CPG circuitry is embedded in the spine. Circuit diagrams of the CPG were proposed in [1]. It therefore appears that this movement is, next to gait, another human CPG.

Objectively, the *standing wave* aspect of the CPG was confirmed by observing that the correlation pattern among the cervical, thoracic, lumbar and sacral surface electromyographic (sEMG) signals is consistent with that of a standing wave. This correlation pattern appears most clearly on the D_8 subband of the Daubechies DB3 wavelet decomposition. The choice of the DB3 wavelet decomposition is justified because its mother function mimics the single motor unit action potential, and the D_8 subband appeared the most relevant as the electro-physiological phenomena appear on that subband while the D_1, D_2, ... subbands are composed mostly of noise [1].

A standing wave oscillation is certainly a manifestation of *coherence* in the neuro-skeletal system. Since the spinal standing wave has its coherence extending from the neck to the sacrum, it is fair to say that this is a phenomenon of *coherence at a distance* [5]. Coherence at a distance between EEG and/or (s)EMG signals is considered to be an attribute of a properly functioning nervous system, as already argued in [5]. The additional evidence that we presented in support of this paradigm is the deterioration of coherence in a quadriplegic subject compared with a control subject [1].

1.2. Contribution

The purpose of this paper is three-fold. First ("Case Study I"), we show that the early results [1] upon which the CPG hypothesis rests are reproducible. Second ("Case Study II"), we show that the spinal wave CPG, in addition to the classical attributes associated with a CPG, can undergo "bifurcation," here understood in a signal processing sense and not in a strict dynamical sense. Finally, another contribution is to show how to deal with signals less than ideal, as those of [1] were.

1.2.1. Reproducibility

Nearly 10 years separate the data collection upon which [1] is based from the present one. During that time, the entrainment technique evolved to make the movement better controllable (the sEMG signals can be made smooth or bursty at will), the electrode positioning underwent some slight changes while we experienced with different orientation of the differential amplifier input prongs relative to muscle fibers, and the hardware (front-end electronics together with sEMG amplifiers) was upgraded. The software underwent some upgrade as well. Despite these changes and a 10-year span between the two experiments, we show in "Case Study I" that the early results [1] upon which the CPG hypothesis rests are reproducible, opening the road for the potential of this coherence analysis to become part of the neurological suite.

1.2.2. Bifurcation

In Case Study II, we add another attribute that can be associated with a CPG: the ability to undergo "bifurcations." The early clues that pointed to such a phenomenon were visually obvious discontinuities in the sEMG signal, an example of which is shown in Figure 1. More formally, here, bifurcation is defined as qualitative structural change; more specifically in the context of the *the standing wave* CPG, bifurcation is typically a change in the mode shape, concomitant with a change in the frequency of the coherent oscillations. From a signal processing view point, this amounts to a shift in the cross power spectral

density of the signals at a distance, something that we endeavor to confirm with inferential statistics. In the topological versus qualitative classifications of [6], our definition of "bifurcation" rather matches a "qualitative" trait of [6]. However, as we shall see, our bifurcation resembles the reverse of the well-known "period doubling" phenomenon, so that it has some of the attributes of a topological bifurcation.

Another sign of this bifurcation phenomenon is a shift of the coherent oscillations from the D_8 to the D_7 subbands of the DB3 wavelet decomposition. As the difference between D_8 and D_7 is a matter of time scale, this is certainly consistent with the shift of the mean in the cross spectral densities, but developing a test of hypothesis of the latter seems extremely difficult at this stage.

Existence of bifurcations should not be that surprising for such a complex system as the human spinal neuro-skeletal system. It simply cannot be expected to oscillate at a single eigenmode and such factors as breathing, even thought processes, have the potential to change the oscillation structural properties. Many such bifurcations on other subjects have already been observed [7**?**] using different methods though. In particular, another bifurcation from 1 to 2 mode shape nodes was already confirmed, using ARIMA modeling [7] of the SAS statistical package.

1.2.3. Less than ideal signals

In the case the signals are analyzed across a bifurcation, the correlation pattern that reveals coherence cannot be expected to be as crisp as that of [1], which can be considered as an ideal, "textbook" example. As such, another purpose of Case-Study II of the present paper is to assess by how much the correlation pattern deviates from those of [1] when conditions are no longer ideal.

2. Methods

The control subjects of the two cases studies presented here are both healthy individuals who, prior to recordings, had signed the informed consent form

approved by the Institutional Review Board (IRB) of the University of Southern California. Surface Electromyography (sEMG) reduced-noise tripolar electrodes were placed at cervical (C2-C3), thoracic (T4-T6), lumbar (L3), and sacral (S2-S4) positions. The sensitive input prongs of the front-end electronics were aligned with the back muscle fibers [8]. The sEMG signals were amplified by an Insight Subluxation Station, Discovery model. The analog-to-digital conversion was done by a USB-1608FS card manufactured by Measurement Computing$^{\text{TM}}$ and running on a Windows XP platform.

During Case Study I, 720,000 samples were recorded at a rate of 4 kHz as shown in Figure 1. The analysis was centred around a section of 100,000 samples, where a phenomenon of synchronicity of signals is visually evident from Figure 2, between 340,000 and 350,000 samples of raw sEMG data.

The procedure for Case Study II, Fig. 1, was similar. Three seconds of data were analyzed using the same sampling rate as Case Study I. This section comprises a set of 12,000 samples, in which the bifurcation is present.

To highlight the differences between the protocol of the earlier study [1] and the protocol utilized to collect the data of Case-Studies I & II, we observe, first, that the sensitive prongs of the electrode front-end electronics were put at a 45 deg. angle relative to spine in the earlier study, as opposed to aligned with the fibers here. Second, the sacral electrode was positioned on the gluteus, as opposed to the sacrum as reported here. Third, the sEMG signals were amplified by an older Insight Millennium sEMG machine and the analog-to-digital conversion was done with a PC-Card DAS16/16, manufactured by Computer Boards (now Measurement Computing$^{\text{TM}}$), running on a Windows 98 operating system, as opposed to the upgraded equipment utilized here.

The fundamental process in the sEMG signal analysis is the Daubechies DB3 wavelet decomposition. This decomposition is chosen because its mother function mimics the single motor unit action potential. Among the many subbands, it is claimed, as in [1], that the D_8, D_7 are the relevant ones. It can indeed be seen from Fig. 2 of [1] that the specificity of the spinal wave shows at D_7, D_8. It is in D_7, D_8 that the electrophysiology shows in synchronization doublets [2].

Let $y_1(k)$, $y_2(k)$, $y_3(k)$, $y_4(k)$ be either the D_8 or the D_7 subband of the cervical, thoracic, lumbar and sacral signals, resp., sEMG signals. As in [1], we define the correlations

$$r_{ij}(s) = \frac{\sum_{k=1}^{K-s}(y_i(k)-\bar{y}_i)(y_j(k+s)-\bar{y}_j)}{\sqrt{\sum_{k=1}^{K-s}(y_i(k)-\bar{y}_i)^2}\sqrt{\sum_{k=1}^{K-s}(y_j(k)-\bar{y}_j)^2}}$$

As argued in [1], the movement has a coherent standing wave if there exist some delays $s_1 < s_2 < \ldots$ such that

$$r_{ij}(s_\ell) = 0; \qquad i,j = 1,2,3,4; \qquad \ell = 1,2,\ldots$$

The points s_ℓ, $\ell = 1,2,\ldots$, have been called *zero correlation nodes* and are manifestations of a coherent standing wave. Clearly, one cannot expect a perfectly coherent standing wave and the above will not, in general, hold for all ℓ's. In practice, one can expect the above to hold reasonably accurately for $\ell = 1$; the accuracy already deteriorates for $\ell = 2$, and in general we no longer look at the above for $\ell > 2$.

3. Results: Case Study I

The raw sEMG signals from the 4 electrodes are shown in Figure 1.

Eyeball inspection of the sEMG traces of Figure 1 already shows some coherence as there is evidence that the signals are bursting synchronously. For example, it suffices to look at the simultaneous bursting of 3 signals around 700,000 samples to see some coherence. However, for the sake of the coherence analysis, we focus our attention on the segment between samples 270,000 and 370,000. This section of raw sEMG is plotted in Figure 2

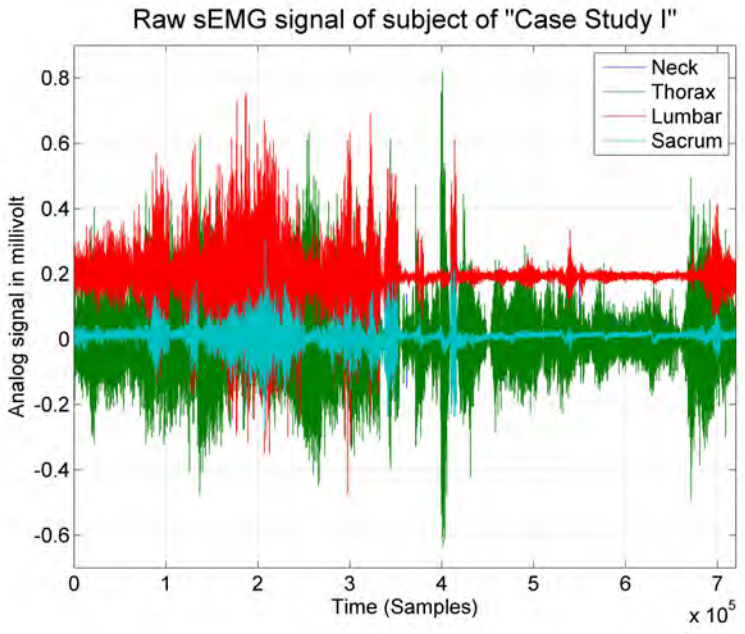

Figure 1: Raw sEMG data at Neck, Thorax, Lumbar and Sacrum of Case Study I

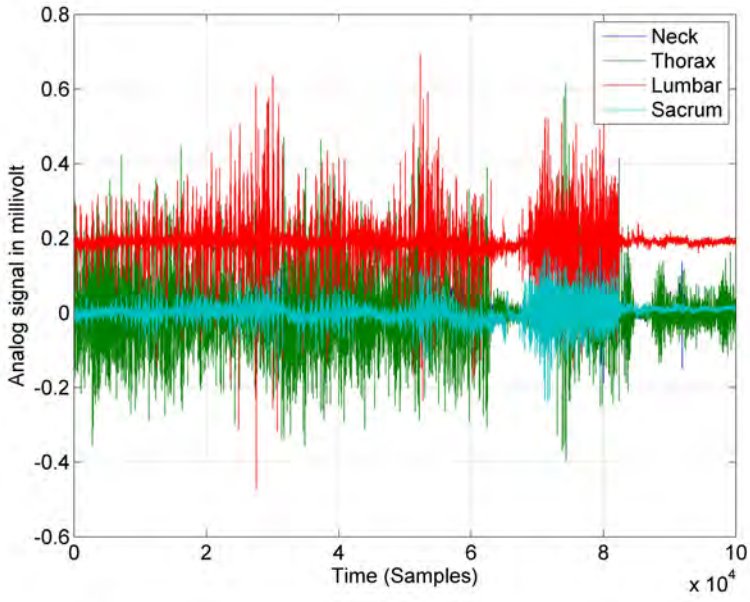

Figure 2: Section from sample 270,000 to 370,000 of raw sEMG data of Case Study I at Neck, Thorax, Lumbar and Sacrum

Again, some synchronous bursting is visually obvious from Figure 2. Note that this bursty signal does not look quite like the one of Figure 1 of [1], which is much smoother. Nevertheless, the coherence results *remain qualitatively the same.*

As argued in [9], from the Daubechies DB3 wavelet decomposition, the signals in the D_1 to D_5 subbands are not of interest because they consist primarily of high frequency noise, where the D_7 and D_8 components show more clearly the "wavelet packets," and D_8 exhibits the better correlation properties.

A summary of the D_8 subbands of the neck to sacrum signals is shown in Figure 3. Most importantly, observe—quite consistently with Figure 2 of [1]—the synchronization doublet of the sacral signal (marked with a circle and identified with a diamond $\diamondsuit$).

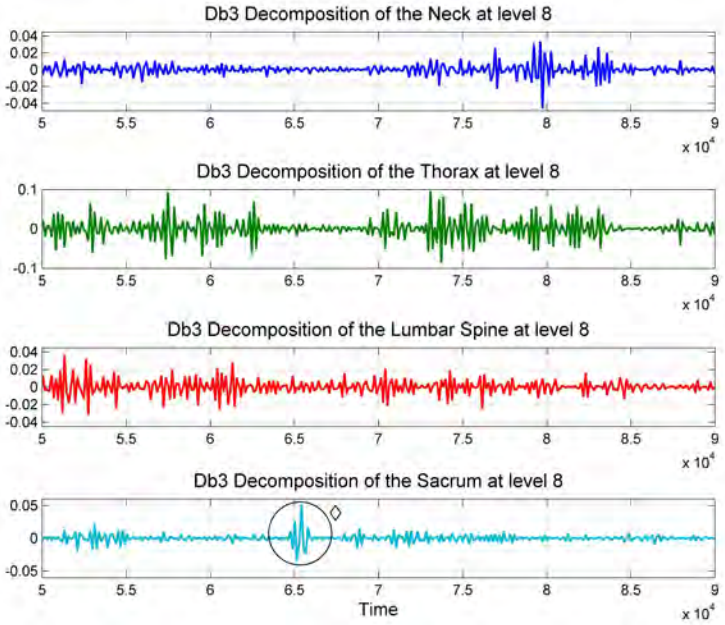

Figure 3: D_8 subbands of Daubechies DB3 wavelet decomposition of Neck, Thorax, Lumbar and Sacrum, respectively

The cross-correlation between the four different sEMG signals obtained from subband D_8 is shown in Figure 4.

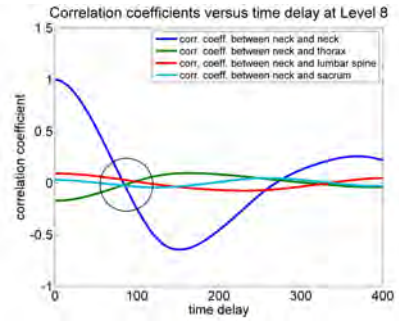

(a) Correlation between D_8 subbands of neck and other signals of control

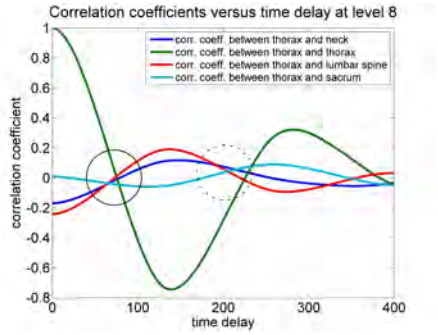

(b) Correlation between D_8 subbands of thorax and other signals of control

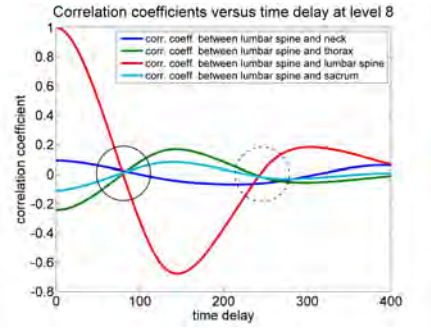

(c) Correlation between D_8 subbands of lumbar and other signals of control

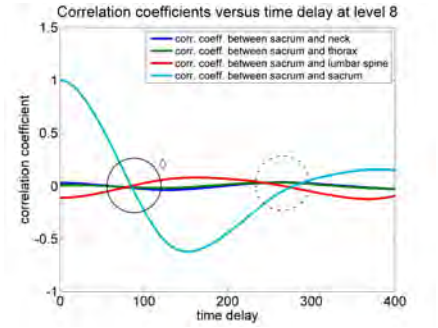

(d) Correlation between D_8 subbands of sacrum and other signals of control

Figure 4: Correlation on D_8 subband among the 4 signals from sample 270,000 to 370,000 of Case Study I.

The plots from Figures 4a-4d are quite similar to those of the left panels of Figures 3-6 of [1]. The s_1 zero correlation nodes (marked with black circles) develop with the same level of accuracy as in [1], while the s_2 nodes (marked with dotted circles) can be seen, but not as markedly as the s_1 node, exactly as in [1].

4. Results: Zero correlation nodes: Case Study II

The raw sEMG data recorded for this case study is shown in Figure 5 for neck and thorax signals.

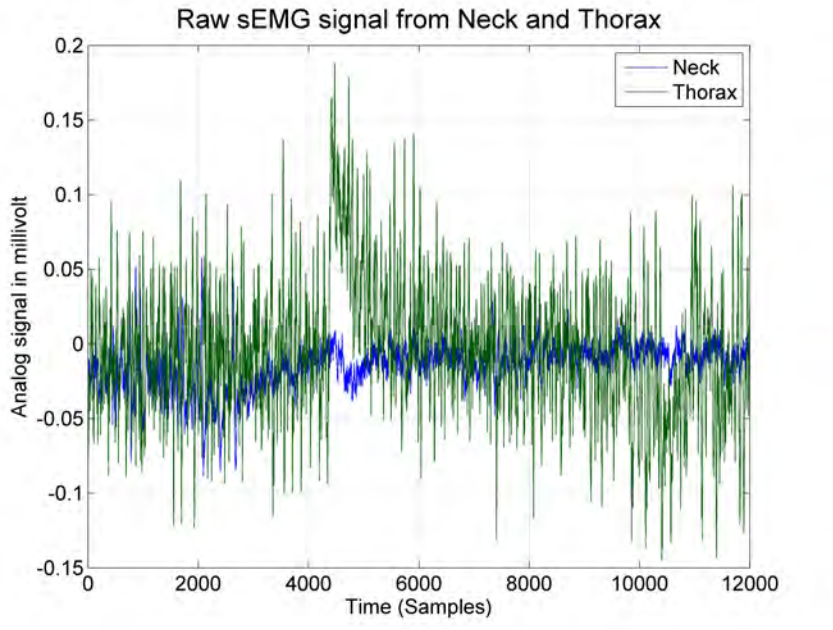

Figure 5: Raw sEMG data obtained from Neck and Thorax, of Case Study II.

Between samples 4,300 and 5,300, the signals exhibit a clear discontinuity, with an obvious lack of correlation between the neck and the thorax signals. Remarkably, this discontinuity in the sEMG traces occurred *exactly* at the time the practitioner, who had no visual contact with the real-time oscilloscopic display of the sEMG signals, called a visually observable change in the structural properties of the spinal wave.

The analysis is broken down in two parts: first, "before the bifurcation," i.e., from sample 1 until sample 4,000; second, "after the bifurcation," that is, between sample 5,411 and sample 9,871. Thus, the specific section comprised within the bifurcation, namely, between samples 4,300 and 5,300, is deliberately avoided, because the standing momentarily disappears and the signals are no longer stationary.

4.1. Analysis before the bifurcation

The specificity of the sEMG signals is observed in the wavelet decomposition on the relevant D_6, D_7 and D_8 subbands of the DB3 decomposition, as it is shown in Figures 6, 7, 8 and 9. The cases of synchronization doublets consistent with zero correlation nodes are identified with circles.

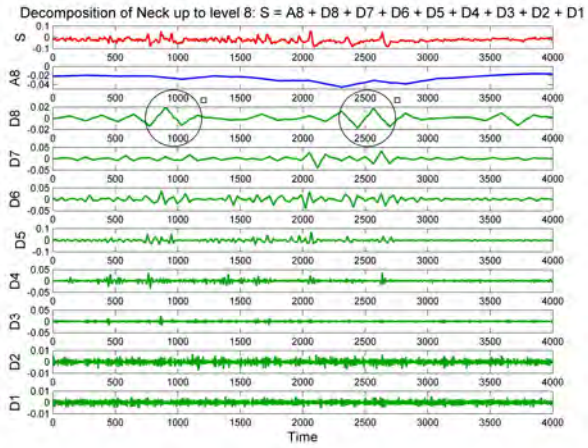

Figure 6: DB3 decomposition of Neck signal before the bifurcation of Case Study II.

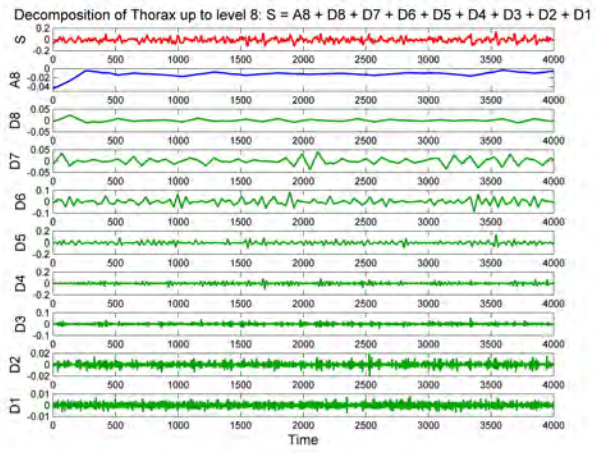

Figure 7: DB3 decomposition of Thorax signal before the bifurcation of Case Study II.

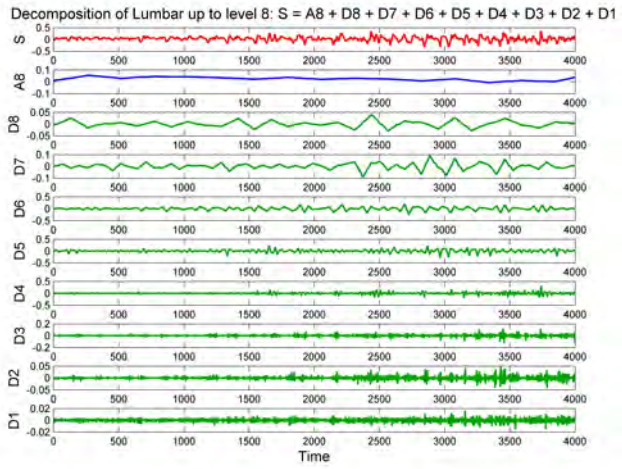

Figure 8: DB3 decomposition of Lumbar signal before the bifurcation of Case Study II.

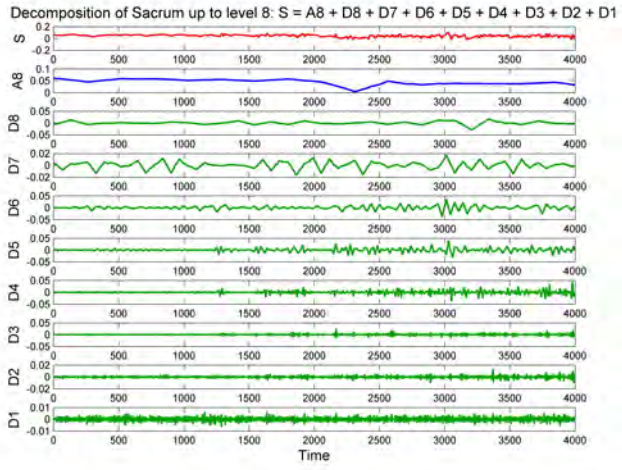

Figure 9: DB3 decomposition of Sacral signal before the bifurcation of Case Study II.

A top (neck) to bottom (sacrum) summary redisplay of this wavelet decomposition before the bifurcation on the relevant D_8, D_7 and D_6 subband signals

is shown in Figures 10, 11 and 12 respectively. Again, the synchronization doublets consistent with zero correlation nodes are identified with circles.

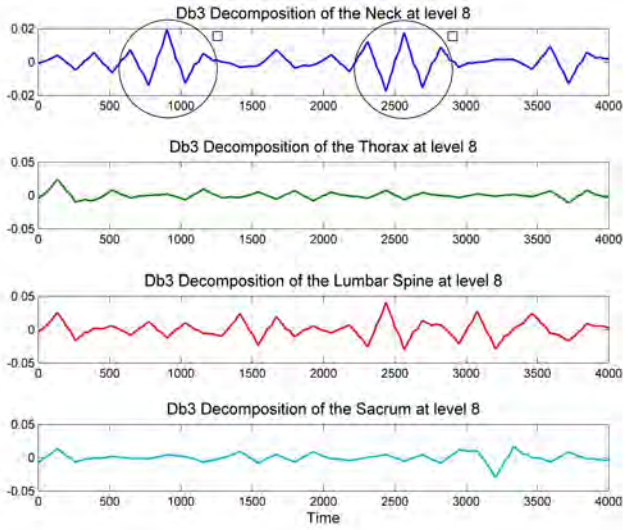

Figure 10: DB3 decomposition of top to bottom signals on D_8 subband before the bifurcation of Case Study II.

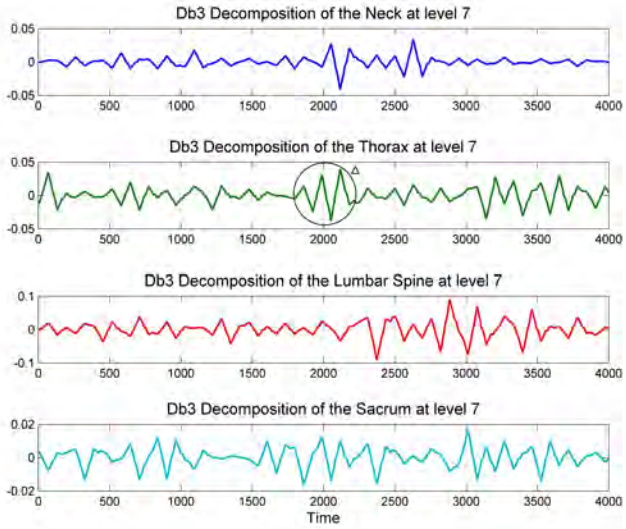

Figure 11: DB3 decomposition of top to bottom signals on D_7 subband before the bifurcation of Case Study II.

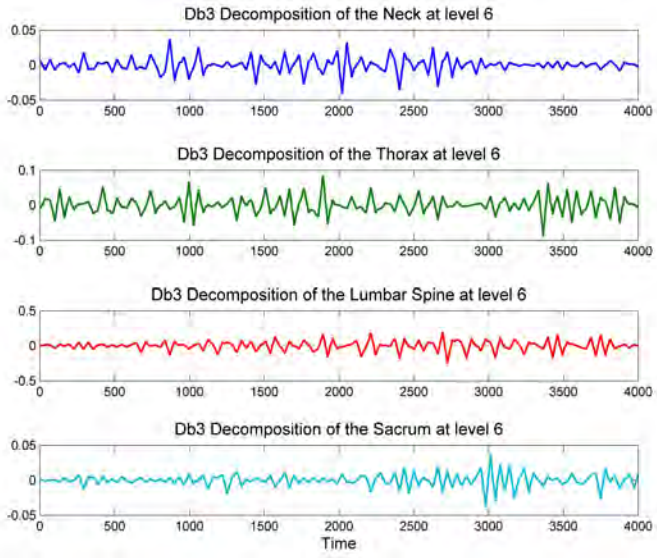

Figure 12: DB3 decomposition of top to bottom signals on D_6 subband before the bifurcation of Case Study II.

The correlation plots before the bifurcation of the D_6, D_7, D_8 subbands are shown in Figures 13, 14 and 15, respectively. The thoracic correlation plot (Figure 13b) does not show coherence at the D_8 subband, in contrast with the other three signals. Complementary to this observation, the correlation of the thorax is at the D_7 subband, which exhibits a better defined zero correlation node as shown in Figure 14b and labeled with a triangle $\triangle$. The sacral curve shows some aberration because of the sacral electrode positioning (not the same as that of [1].) On the D_7, not much correlation can be seen, except for the thoracic plot. On the D_6, not much correlation can be seen. (On the lumbar plots, there *appears* to be a crossing, but it is too far off the $r = 0$ axis to be of any significance.)

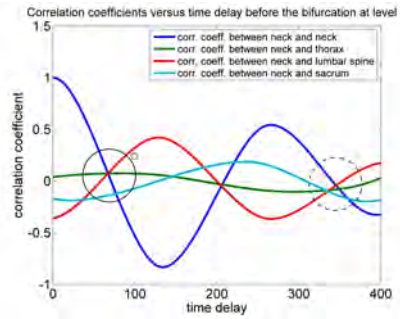

(a) Correlation between D_8 subbands of neck and other signals of control

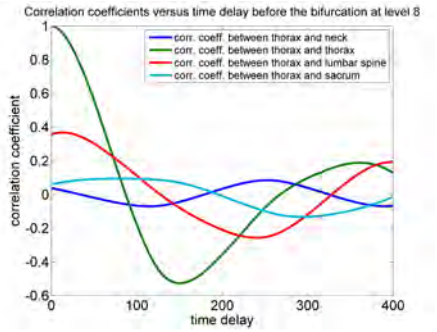

(b) Correlation between D_8 subbands of thorax and other signals of control

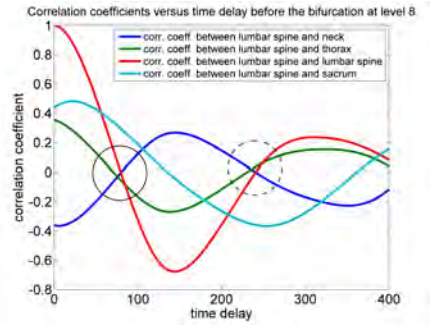

(c) Correlation between D_8 subbands of lumbar and other signals of control

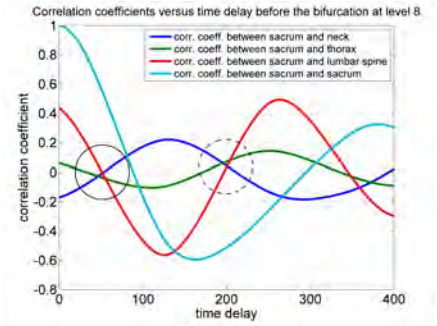

(d) Correlation between D_8 subbands of sacrum and other signals of control

Figure 13: Correlation on D_8 subband of top to bottom signals before the bifurcation of Case Study II.

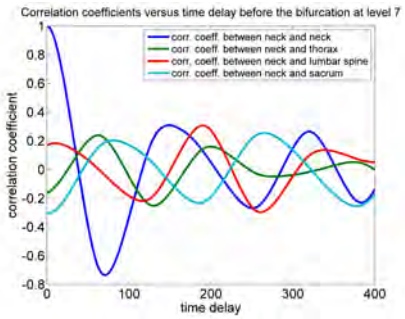

(a) Correlation between D_7 subbands of neck and other signals of control

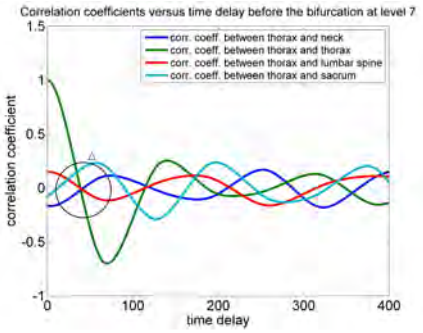

(b) Correlation between D_7 subbands of thorax and other signals of control

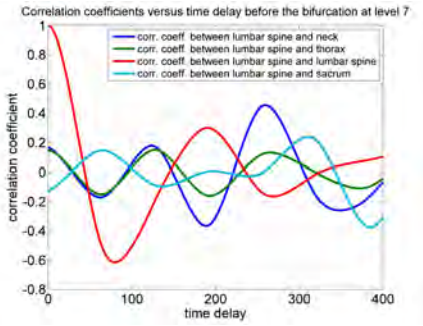

(c) Correlation between D_7 subbands of lumbar and other signals of control

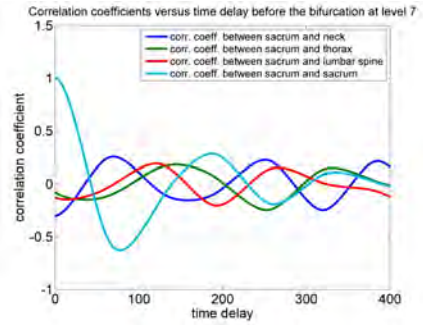

(d) Correlation between D_7 subbands of sacrum and other signals of control

Figure 14: Correlation on D_7 subband of top to bottom signals before the bifurcation of Case Study II.

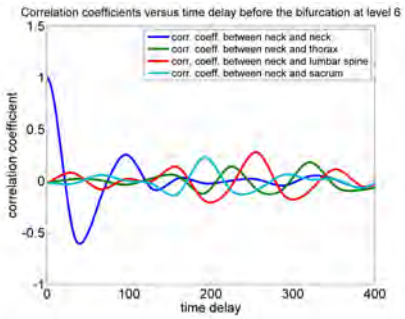

(a) Correlation between D_6 subbands of neck and other signals of control

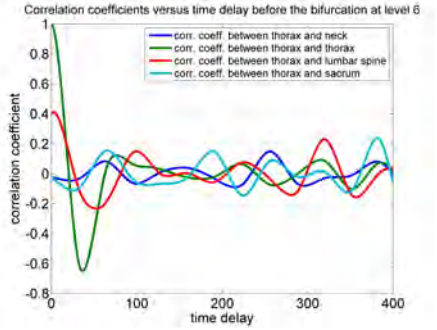

(b) Correlation between D_6 subbands of thorax and other signals of control

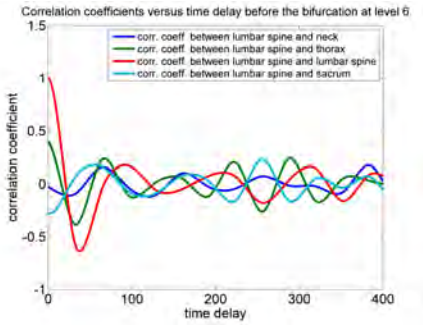

(c) Correlation between D_6 subbands of lumbar and other signals of control

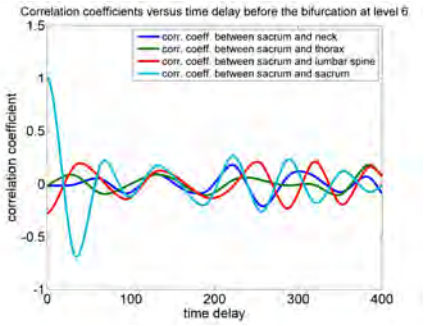

(d) Correlation between D_6 subbands of sacrum and other signals of control

Figure 15: Correlation on D_6 subband of top to bottom signals before the bifurcation of Case Study II.

4.2. Analysis after the bifurcation

The same procedure was performed right after the section where the bifurcation phenomenon terminates, and comprises approximately one second of the sEMG trace, (from 5,411 to 9,871 samples). As in the previous case (before the bifurcation), the wavelet packets were also best observed on the D_8, D_7 and D_6 subbands. The corresponding correlation plots after the bifurcation are shown in Figures 16, 17 and 18.

On the D_8 subband, not much correlation can be seen, except possibly on the sacral curves (see black circle). On the other hand, the D_7 subband shows

several s_1 nodes and even higher zero crossing nodes. The D_6 does not appear to show any zero correlation nodes.

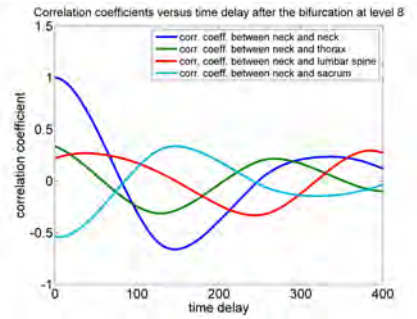

(a) Correlation between D_8 subbands of neck and other signals of control

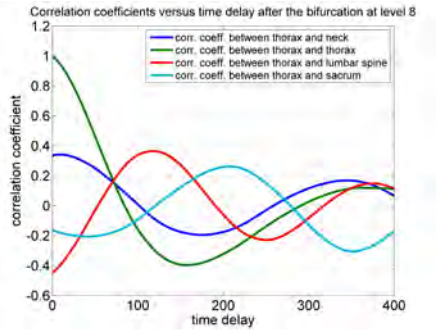

(b) Correlation between D_8 subbands of thorax and other signals of control

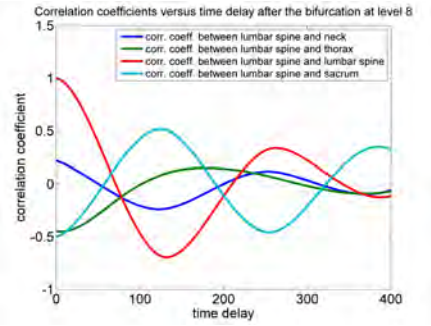

(c) Correlation between D_8 subbands of lumbar and other signals of control

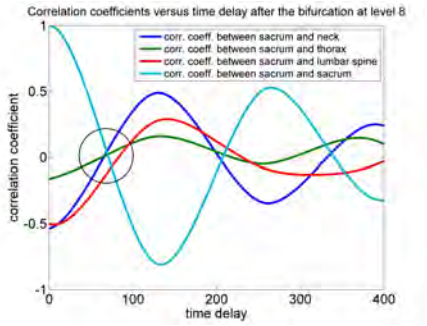

(d) Correlation between D_8 subbands of sacrum and other signals of control

Figure 16: Correlation plots on D_8 subband of top to bottom signals after the bifurcation of Case Study II.

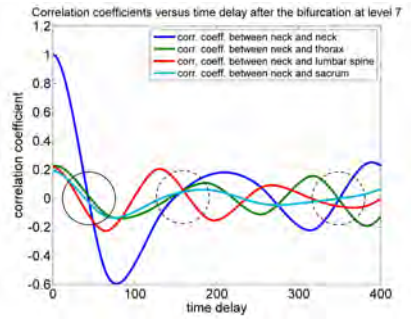

(a) Correlation between D_7 subbands of neck and other signals of control

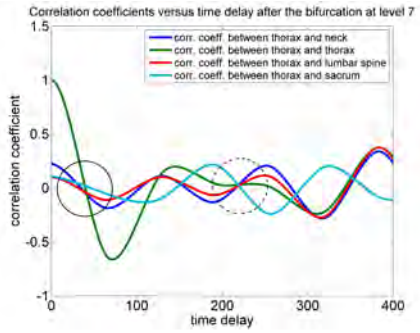

(b) Correlation between D_7 subbands of thorax and other signals of control

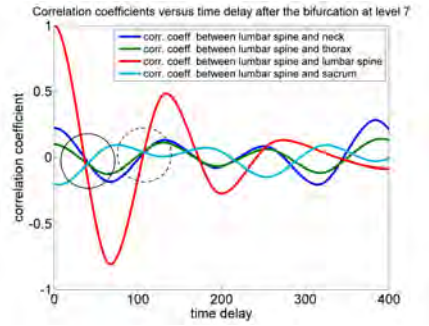

(c) Correlation between D_7 subbands of lumbar and other signals of control

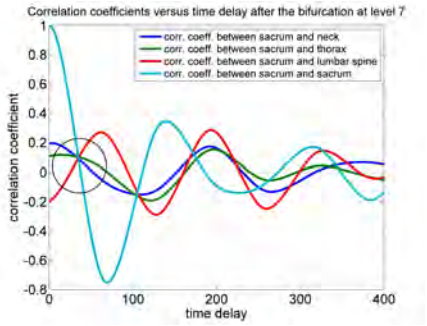

(d) Correlation between D_7 subbands of sacrum and other signals of control

Figure 17: Correlation plots on D_7 subband of top to bottom signals after the bifurcation of Case Study II.

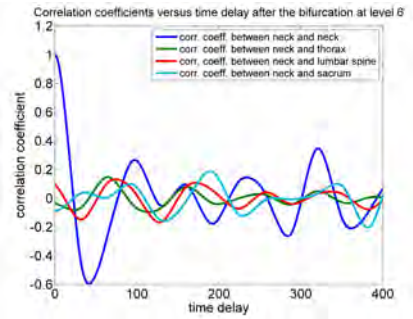

(a) Correlation between D_6 subbands of neck and other signals of control

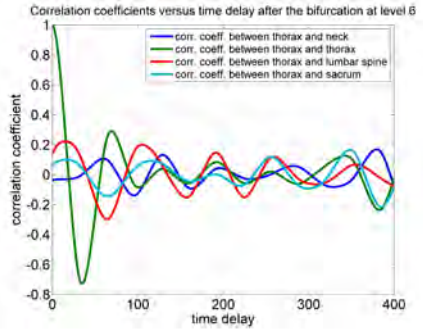

(b) Correlation between D_6 subbands of thorax and other signals of control

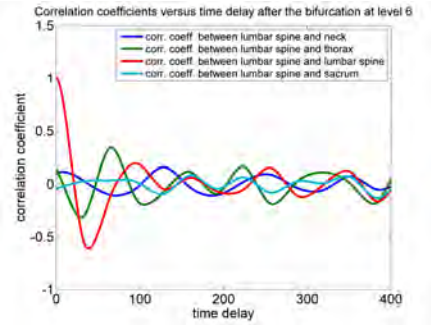

(c) Correlation between D_6 subbands of lumbar and other signals of control

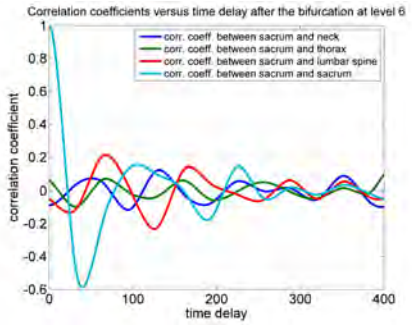

(d) Correlation between D_6 subbands of sacrum and other signals of control

Figure 18: Correlation plots on D_6 subband of top to bottom signals after the bifurcation of Case Study II.

5. Results: Shift in cross spectral density: Case Study II

It can be observed in Figures 13, 14, 16 and 17 that the "slow" D_8 sub-band shows larger correlation than the D_7 sub-band *before the bifurcation*, and the "faster" D_7 sub-band shows larger correlation than the D_8 sub-band *after the bifurcation*. Thus, we expect the *cross Power Spectral Density (cPSD)* between two signals along the spine to be larger in high frequency *after the bifurcation*. Equivalently, we expect the *cPSD* to be larger in low frequency *before the bifurcation*. This "educated guess" is supported by the data from the lower spinal

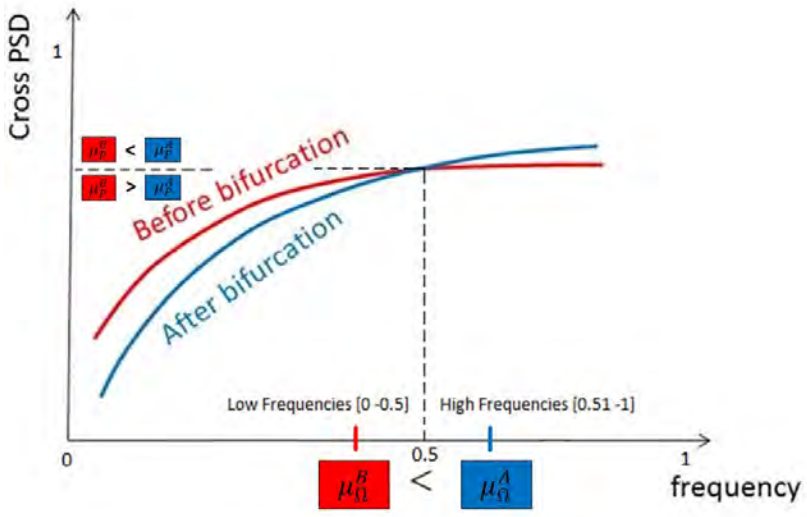

Figure 19: Qualitative behavior of the cross Power Spectral Densities (cPSDs) against the frequency for the lower spine signals Before (red) and After (blue) the bifurcation

signals and is confirmed by a statistical test of significance, which we endeavored to develop specially for this specific problem.

After obtaining the cPSD of the spine signals, that is, the frequency distribution of the 16 possible cases of correlation between two signals out of the four (cervical, thoracic, lumbar, and sacral) spine signals, we come up with a *qualitative* behavior of the cPSD across the bifurcation for the lower spinal signals as shown in Figure 19. The randomness is analyzed in terms of the normalized cPSD distributions, and we define the "Before" and "After" probability density functions, $f_P^B(\rho)$, $f_P^A(\rho)$, respectively. Let μ_P^B, μ_P^A be the means of $f_P^B(\rho)$, $f_P^A(\rho)$, respectively. To statistically demonstrate the existence of the intersection between the red and blue curves of Figure 19, the test was broken down into low normalized frequencies, from 0 to 0.5, and high normalized frequencies, from 0.51 to 1. From this standpoint, it suffices to show that, statistically, there is enough confidence in asserting that $\mu_P^B < \mu_P^A$ at high frequencies and $\mu_P^B > \mu_P^A$ at low frequencies.

5.1. Prelude: test of significance under Gauss assumption

Since we focus our attention on the randomness defined by the cPSD values, we statistically define $\rho_1^B, \rho_2^B, \rho_3^B, \ldots, \rho_m^B$ as a random draw from $f_P^B(\rho)$ and $\rho_1^A, \rho_2^A, \rho_3^A, \ldots, \rho_m^A$ as a random draw from $f_P^A(\rho)$. Define the "Before" and "After" means as

$$\bar{\rho}^B = \frac{1}{m}\sum_{i=1}^{m}\rho_i^B, \qquad \bar{\rho}^A = \frac{1}{m}\sum_{i=1}^{m}\rho_i^A.$$

Define the sample variances:

$$(s^B)^2 = \frac{1}{m-1}\sum_{i=1}^{m}(\rho_i^B - \bar{\rho}^B)^2, \qquad (s^A)^2 = \frac{1}{m-1}\sum_{i=1}^{m}(\rho_i^A - \bar{\rho}^A)^2.$$

It turns out that, under Gauss assumption on the normalized cPSDs $f_P^B(\rho)$ and $f_P^A(\rho)$, the quantity

$$t = \frac{\bar{\rho}^B - \bar{\rho}^A}{\sqrt{\frac{(s^B)^2+(s^A)^2}{m}}}$$

has approximately a t-distribution [10], and becomes Gaussian for m large. We want to show that $\mu_P^B < \mu_P^A$ for f_P^B, f_P^A restricted to high frequencies and $\mu_P^B > \mu_P^A$ for distributions restricted to low frequencies; statistically speaking, $\bar{\rho}^B - \bar{\rho}^A < 0$ at high frequencies and $\bar{\rho}^B - \bar{\rho}^A > 0$ at low frequencies.

The problem is that our investigations have shown that $f_P^B(\rho)$, $f_P^A(\rho)$ *do not* follow the Gauss distribution. Thus, to go around the lack of Gaussian property of $f_P^B(\rho)$, $f_P^A(\rho)$, we need to perform bootstrapping of the cPSD values.

5.2. No Gauss assumption: bootstrapping

Bootstrapping is a Monte Carlo method [11] that employs repeated samples with replacement from the original data. This testing procedure is useful when the theoretical distribution of the statistic is complicated—as in our case—or unknown. Using bootstrapping, we conducted a statistical test of hypothesis to estimate the Achieved Significance Level (ASL) of the test, also known as *p-value*.

We begin by calculating the value of the test statistic for the sample,

$$t_{\text{calc}} = \frac{\bar{\rho}^B - \bar{\rho}^A}{\sqrt{\frac{(s^B)^2+(s^A)^2}{m}}}.$$

Then we transform the m values from the B-sample as $x_i^B = \rho_i^B - \bar{\rho}^B + \bar{\bar{\rho}}$ and those from the A-sample as $x_i^A = \rho_i^A - \bar{\rho}^A + \bar{\bar{\rho}}$, where $\bar{\bar{\rho}} = (\bar{\rho}^B + \bar{\rho}^A)/2$ is the mean of the combined samples; thereafter, we randomly sample $\{x_i^A\}$ and $\{x_i^B\}$ with replacement and repeat the same operation a total of j times.

For each bootstrap sample j, we compute the test statistic

$$t_j = \frac{\bar{x}^B - \bar{x}^A}{\sqrt{\frac{(s^B)^2+(s^A)^2}{m}}},$$

where $\bar{x}^B$ and $\bar{x}^A$ are the means of bootstrap sample j for sample $\{x_i^B\}$ and $\{x_i^A\}$, respectively.

Next, we define the *Null Hypothesis* H_0 as follows:

$$H_0 : (\mu_P^B - \mu_P^A) = 0,$$

and we define the *Alternative Hypotheses* and the bootstrap estimated *p-value* as

$$\text{Upper-tailed test } (H_a : (\mu_P^B - \mu_P^A) > 0): \qquad ASL = \frac{\text{Number of times } t_j > t_{\text{calc}}}{j}$$

$$\text{Lower-tailed test } (H_a : (\mu_P^B - \mu_P^A) < 0): \qquad ASL = \frac{\text{Number of times } t_j < t_{\text{calc}}}{j}$$

"Upper-tailed" ("Lower-tailed") test refers to low (high) frequency restrictions of f_P^B, f_P^A.

The bootstrapping procedure described above was implemented on MatLab, and it was run ten different times for each of the $j = 100$, $j = 1,000$, $j = 10,000$, $j = 100,000$, and $j = 1,000,000$ bootstrap samples from the cPSD of every pair of signals at low and high frequencies. The averages of the p-values and their convergence to a stable value for every j is shown in the Appendix section. In addition, this bootstrap analysis was also run on JMP Pro 11, a statistical software developed by the SAS Institute. Using $j = 10,000$, we obtained similar

p-values as those of the MatLab bootstrap analysis. Both p-values are reported in Tables 1 and 2.

We decided to reject the Null Hypothesis when the p-value fell below 0.05. In Tables 1 and 2, we highlight those cases that significantly concur, with 95% confidence level, with the qualitative behavior gleaned from Figure 19. Clearly, the Alternative Hypothesis holds in just about all cases involving lower spine signals (Table2), whereas the Alternative Hypothesis is a bit problematic for the upper spine signals (Table 1). This can be explained by the fact that the sacral oscillator of [1, Fig. 7] is better engaged that the cervical one.

Upper Spine Signals					
Neck	Neck & Neck BEFORE VS AFTER				
	Frequencies	Alternative Hypothesis	P-values calculated using: MatLab	JMP	Conclusion
	Low	$Ha: \mu_{Before} < \mu_{After}$	0.02815 (S.D. = 0.000212)	0.03	Accept Ha
	High	$Ha: \mu_{Before} > \mu_{After}$	0.00075 (S.D. = 0.0000527)	0.0014	Accept Ha
	Neck & Thorax BEFORE VS AFTER				
	Frequencies	Alternative Hypothesis	P-values calculated using: MatLab	JMP	Conclusion
	Low	$Ha: \mu_{Before} < \mu_{After}$	0.0851 (S.D. = 0.000270801)	0.0861	Accept Ho
	High	$Ha: \mu_{Before} > \mu_{After}$	0.56888 (S.D. = 0.000332666)	0.5678	Accept Ho
	Neck & Lumbar BEFORE VS AFTER				
	Frequencies	Alternative Hypothesis	P-values calculated using: MatLab	JMP	Conclusion
	Low	$Ha: \mu_{Before} < \mu_{After}$	0.04734 (S.D. = 0.000117379)	0.0456	Accept Ha
	High	$Ha: \mu_{Before} > \mu_{After}$	0.0000 (S.D. = 0.0000)	0.0001	Accept Ha
	Neck & Sacrum BEFORE VS AFTER				
	Frequencies	Alternative Hypothesis	P-values calculated using: MatLab	JMP	Conclusion
	Low	$Ha: \mu_{Before} > \mu_{After}$	0.00332 (S.D. = 0.00004216)	0.0030	Accept Ha
	High	$Ha: \mu_{Before} < \mu_{After}$	0.00199 (S.D. = 0.00005676)	0.002	Accept Ha
Thorax	Thorax & Neck BEFORE VS AFTER				
	Frequencies	Alternative Hypothesis	P-values calculated using: MatLab	JMP	Conclusion
	Low	$Ha: \mu_{Before} < \mu_{After}$	0.08504 (S.D. = 0.0002319)	0.0861	Accept Ho
	High	$Ha: \mu_{Before} < \mu_{After}$	0.4311 (S.D. = 0.000505525)	0.4322	Accept Ho
	Thorax & Thorax BEFORE VS AFTER				
	Frequencies	Alternative Hypothesis	P-values calculated using: MatLab	JMP	Conclusion
	Low	$Ha: \mu_{Before} < \mu_{After}$	0.07255 (S.D. = 0.000236878)	0.0725	Accept Ho
	High	$Ha: \mu_{Before} < \mu_{After}$	0.05179 (S.D. = 0.000172884)	0.0517	Accept Ho
	Thorax & Lumbar BEFORE VS AFTER				
	Frequencies	Alternative Hypothesis	P-values calculated using: MatLab	JMP	Conclusion
	Low	$Ha: \mu_{Before} > \mu_{After}$	0.42737 (S.D. = 0.000386005)	0.4271	Accept Ho
	High	$Ha: \mu_{Before} < \mu_{After}$	0.0000 (S.D. = 0.0000)	0.0001	Accept Ha
	Thorax & Sacrum BEFORE VS AFTER				
	Frequencies	Alternative Hypothesis	P-values calculated using: MatLab	JMP	Conclusion
	Low	$Ha: \mu_{Before} > \mu_{After}$	0.0000 (S.D. = 0.0000)	0.0001	Accept Ha
	High	$Ha: \mu_{Before} > \mu_{After}$	0.0000 (S.D. = 0.0000)	0.0001	Accept Ha

Table 1: P-values of the bootstrap statistical test from the upper spine signals

Lower Spine Signals					
Lumbar	Lumbar & Neck BEFORE VS AFTER				
	Frequencies	Alternative Hypothesis	P-values calculated using: MatLab	P-values calculated using: JMP	Conclusion
	Low	$Ha: \mu_{Before} > \mu_{After}$	0.04732 (S.D. = 0.000297396)	0.0456	Accept Ha
	High	$Ha: \mu_{Before} > \mu_{After}$	0.0000 (S.D. = 0.0000)	0.0001	Accept Ha
	Lumbar & Thorax BEFORE VS AFTER				
	Frequencies	Alternative Hypothesis	P-values calculated using: MatLab	P-values calculated using: JMP	Conclusion
	Low	$Ha: \mu_{Before} > \mu_{After}$	0.42693 (S.D. = 0.000678315)	0.4271	Accept Ho
	High	$Ha: \mu_{Before} < \mu_{After}$	0.0000 (S.D. = 0.0000)	0.0001	Accept Ha
	Lumbar & Lumbar BEFORE VS AFTER				
	Frequencies	Alternative Hypothesis	P-values calculated using: MatLab	P-values calculated using: JMP	Conclusion
	Low	$Ha: \mu_{Before} > \mu_{After}$	0.00265 (S.D. = 0.000052704)	0.0025	Accept Ha
	High	$Ha: \mu_{Before} < \mu_{After}$	0.0000 (S.D. = 0.0000)	0.0001	Accept Ha
	Lumbar & Sacrum BEFORE VS AFTER				
	Frequencies	Alternative Hypothesis	P-values calculated using: MatLab	P-values calculated using: JMP	Conclusion
	Low	$Ha: \mu_{Before} > \mu_{After}$	0.0000 (S.D. = 0.0000)	0.0001	Accept Ha
	High	$Ha: \mu_{Before} > \mu_{After}$	0.0033 (S.D. = 0.0000816497)	0.0034	Accept Ha
Sacrum	Sacrum & Neck BEFORE VS AFTER				
	Frequencies	Alternative Hypothesis	P-values calculated using: MatLab	P-values calculated using: JMP	Conclusion
	Low	$Ha: \mu_{Before} > \mu_{After}$	0.00331 (S.D. = 0.000073786)	0.0030	Accept Ha
	High	$Ha: \mu_{Before} < \mu_{After}$	0.002 (S.D. = 0.0000471405)	0.002	Accept Ha
	Sacrum & Thorax BEFORE VS AFTER				
	Frequencies	Alternative Hypothesis	P-values calculated using: MatLab	P-values calculated using: JMP	Conclusion
	Low	$Ha: \mu_{Before} > \mu_{After}$	0.0000 (S.D. = 0.0000)	0.0001	Accept Ha
	High	$Ha: \mu_{Before} > \mu_{After}$	0.0000 (S.D. = 0.0000)	0.0001	Accept Ha
	Sacrum & Lumbar BEFORE VS AFTER				
	Frequencies	Alternative Hypothesis	P-values calculated using: MatLab	P-values calculated using: JMP	Conclusion
	Low	$Ha: \mu_{Before} > \mu_{After}$	0.0000 (S.D. = 0.0000)	0.0001	Accept Ha
	High	$Ha: \mu_{Before} > \mu_{After}$	0.00329 (S.D. = 0.000031622)	0.0034	Accept Ha
	Sacrum & Sacrum BEFORE VS AFTER				
	Frequencies	Alternative Hypothesis	P-values calculated using: MatLab	P-values calculated using: JMP	Conclusion
	Low	$Ha: \mu_{Before} > \mu_{After}$	0.0000 (S.D. = 0.0000)	0.0001	Accept Ha
	High	$Ha: \mu_{Before} > \mu_{After}$	0.0000 (S.D. = 0.0000)	0.0001	Accept Ha

Table 2: P-values of the bootstrap statistical test from the lower spine signals.

6. Discussion: Zero correlation nodes: Case Study I

Observe in Figure 4 the well-defined "zero correlation nodes" i.e., the common points of intersection of all the $r_{ij}(s)$ versus s curves and the $r = 0$ axis, strong evidence of a coherent standing wave. Both the s_1 nodes and to a less extent the s_2 nodes are visible (marked with solid and dotted circles, resp.). Also note the consistency between the synchronization doublet of Figure 3, sacrum, and the s_1 node of Figure 4, sacrum (d), both of them identified with a diamond $\diamondsuit$. As such, it is fair to say that the results of [1] have been reproduced in an

environment deliberately taken not as "clean" as that of [1].

However, the same results are not as visually obvious for Case Study II when a "bifurcation" occurs.

7. Discussion: Case Study II

Before the bifurcation, the "zero correlation nodes" are somehow clear on the D_8 subband as shown in Figure 13, but markedly depleted on the D_7 and D_6 subbands, as shown in Figures 14 and 15, respectively.

Observe the consistency between the synchronization doublets of Figure 10 and the s_1 node of Figure 13, neck (a), marked with a box $\Box$. We have the same consistency between the synchronization doublets of Figure 11 and the s_1 node of Figure 14, thorax (b), marked with a triangle $\triangle$.

After the bifurcation, the D_8 subband is no longer the best to reveal coherence as shown in Figures 16a-16d. Contrarily to [1] and Case-Study I of the present paper, the D_7 subband of the signals restricted from sample 5,411 to 9,871 exhibits better zero correlation nodes as shown in Figures 17a-17d.

The qualitative behavior of Figure 19 happens to be consistent for the lower spinal signals, as demonstrated by the statistical test of significance, where a depletion of the low frequency component occurs predominantly *after the bifurcation*. Furthermore, this statistical test corroborates the zero correlation nodes pattern that takes place on two different subbands when the system passes through a bifurcation.

It is thus fair to say that, before the bifurcation, the coherence is at the D_8 level, while, after the bifurcation, the coherence is at the D_7 level.

Comparing the D_8 and the D_7 correlation plots, it is clear that the latter reveal a coherent movement twice as fast as the former. Therefore, the passage from a coherence standing wave on D_8 to a coherent standing wave on D_7 means that the standing wave doubles its speed across the bifurcation. This phenomenon is somehow the reverse of the well-known period doubling phenomenon in chaos [12].

8. Conclusion

First, in Case Study I, we illustrated the reproducibility of the results of [1], indicating that the spinal wave is a coherent movement elicited by a Central Pattern Generator. Here *reproducibility* spans across a period of more than 10 years, during which many changes in the protocol and the experimental hardware occurred, hence demonstrating the "robustness" of the results. Ref. [1] as well as Case-Study I have demonstrated coherence at the D_8 subband of the DB3 wavelet decomposition. Second, the really novel result here is the observation that the standing wave, revealing the neuro-physiologically relevant coherence at a distance [5], can undergo a bifurcation with a shift of the coherence from D_8 to D_7. More practically speaking, this means that the motion speeds by a factor of 2, in a process that appears to be the reverse of the well-known period doubling [13] in dynamical systems theory. One interpretation of this finding could be a higher tension pattern in the spine elicited after the bifurcation. From a more conceptual point of view, a reverse period doubling is transition *away* from chaos. We have observed by working on quadriplegic patients that in general their sEMG signals are more chaotic than control subjects. Thus the bifurcation might be interpreted as the nervous system going to a less chaotic attractor.

The statistical test of the shift of the mean of the cross Power Spectral Density corroborates the shift of the zero correlation nodes from the D_8 subband, before the bifurcation, to the D_7 subband, after the bifurcation. This statistical test confirms a structural change in the power spectrum of the signal as the system passes through a reverse period doubling bifurcation; at low frequencies the power of the signal before the bifurcation turned out to be statistically significantly higher than the power of the signal after the bifurcation, with a 95% confidence level. The latter is to be interpreted with the restriction that this happens to be prevalent among the lower spine signals (lumbar spine and sacrum), when the sacral oscillator is better engaged than the cervical one.

It is hoped that the fundamental technique developed in this paper—the

combination of coherence at D_8 versus D_7 together with inferential statistics on the shift of the mean of the cross power spectral densities—will be applicable to confirm other bifurcations, which as already argued are likely to happen in such complex neuro-skeletal systems.

Finally, while coherence at a distance is recognized to be a sign of neuro-physiological system health [5], the more subtle features of whether coherence occurs at D_8 or D_7, or possibly at yet another subband, and how easily/how difficult it is for the neuro-physiological system to undergo the bifurcations remain to be assess in terms of their physiological relevance.

Acknowledgment

Dr. Kosko's help in developing the test of Section 5.2 is gratefully acknowledged.

References

[1] E. Jonckheere, P. Lohsoonthorn, S. Musuvathy, V. Mahajan, M. Stefanovic, On a standing wave central pattern generator and the coherence problem, Biomedical Signal Processing and Control (2010) 336–347.

[2] N. Kopell, We got rhythm: Dynamical systems of the nervous system, Notices of the American Mathematical Society 47 (1).

[3] A. Breig, Adverse Mechanical Tension in the Central Nervuous System, John Wiley, New York, 1987.

[4] A. Tilton, P. G. Mehta, Control with rhythms: A CPG architecture for pumping a swing, in: American Control Conference (ACC), Portland, Oregon, USA, 2014.

[5] S. F. Farmer, Rhythmicity, synchronization and binding in human and primate motor systems, The Journal of Physiology 509 (1998) 3–14.

[6] Y. A. Kuznetsov, Elements of Applied Bifurcation Theory. Applied Mathematical Sciences, Vol. 112, Springer-Verlag New York, Inc., 1998.

[7] E. Jonckheere, P. Lohsoonthorn, R. Boone, Dynamic modeling of spinal electromyographic activity during various conditions, in: NSF Southwest Regional Workshop on New Directions in Dynamical Systems, University of Southern California, Los Angeles, 2003.

[8] S. Day, Important factors in surface emg measurement, Tech. rep., Bortec Biomedical Ltd, 225, 604-1st St. Sw, Calgary, AB, T2P 1M7, Canada (2000).

[9] E. A. Jonckheere, P. Lohsoonthonrn, Spatio-temporal analysis of an electrophysiological wave phenomenon, Leuven, Belgium, 2004.

[10] M. G. Bulmer, Principles of Statistics, Dover, 1979.

[11] W. Mendenhall, T. Sincich, Statistics for Engineering and the Sciences, 5th Edition, Prentice Hall, 2007.

[12] T. Tel, M. Gruiz, Chaotic Dynamics: An Introduction Based on Classical Mechanics, Cambridge University Press, Budapest, 2006.

[13] D. W. Berns, J. L. Moiola, G. Chen, Predicting period-doubling bifurcations and multiple oscillations in nonlinear time-delayed feedback systems, IEEE Transactions on Circuits and Systems I: Fundamental Theory and Applications 45 (7).

Appendix A. Statistical Test. Convergence of p-values.

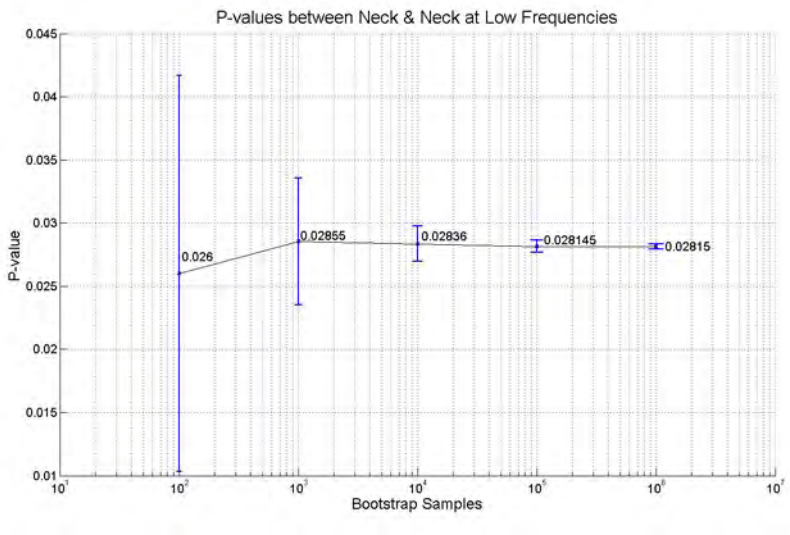

Figure Appendix A.1: Convergence at 0.02815 of the p-value between Neck and Neck at low frequencies.

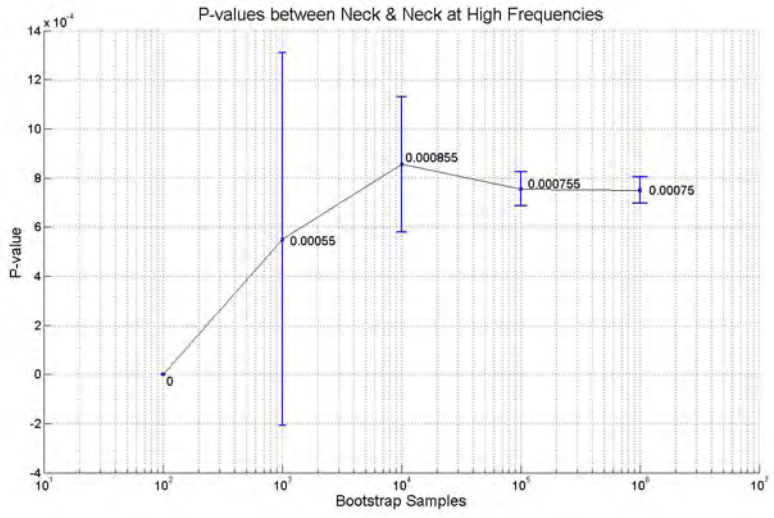

Figure Appendix A.2: Convergence at 0.00075 of the p-value between Neck and Neck at high frequencies.

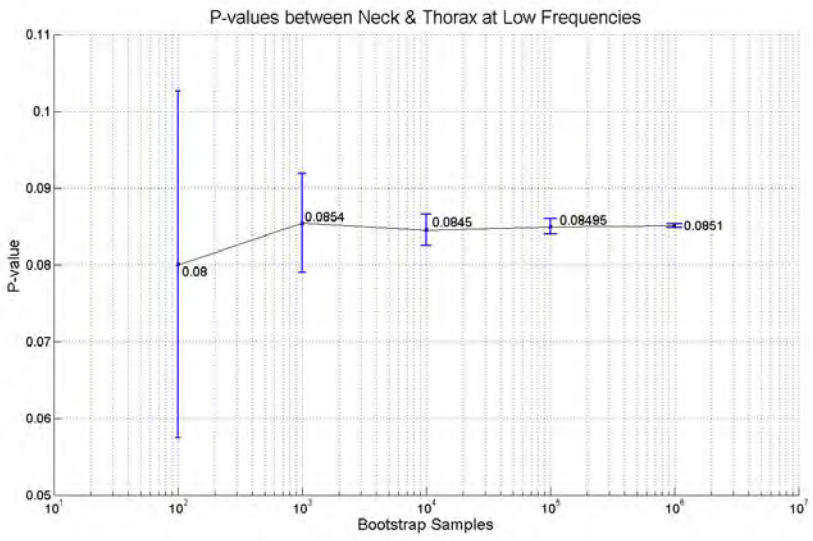

Figure Appendix A.3: Convergence at 0.0851 of the p-value between Neck and Thorax at low frequencies.

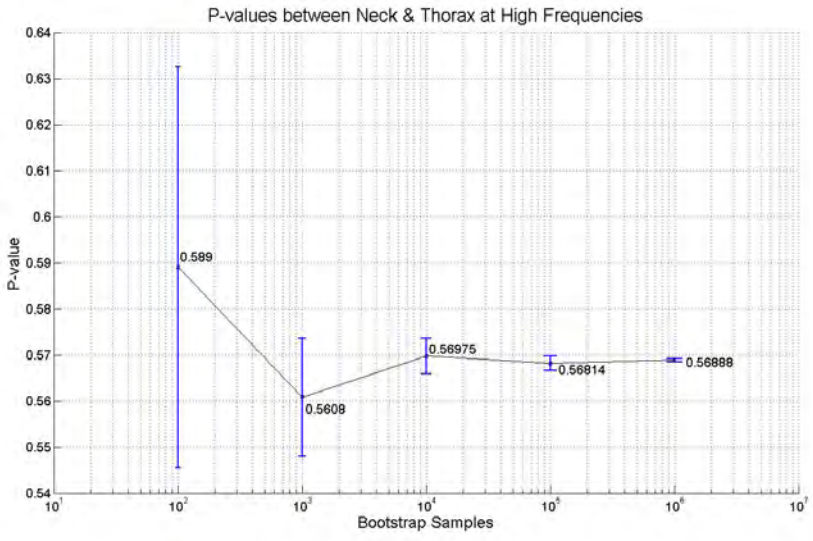

Figure Appendix A.4: Convergence at 0.56888 of the p-value between Neck and Thorax at high frequencies.

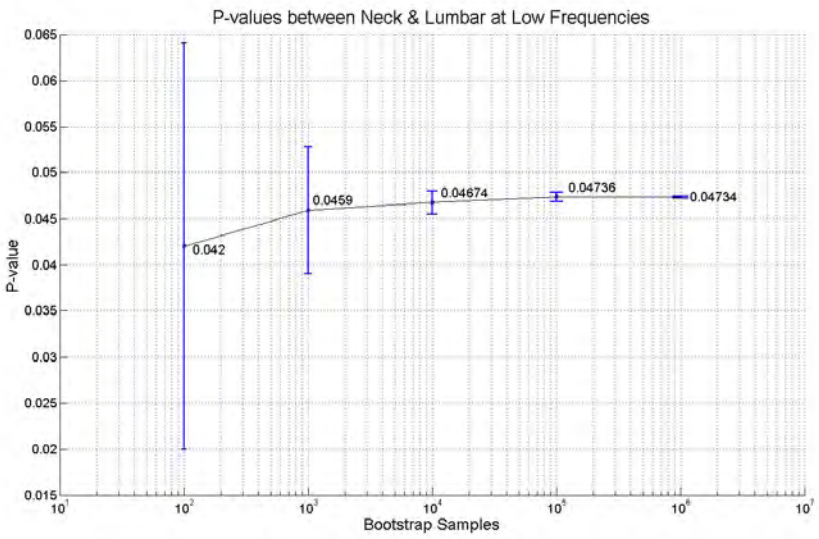

Figure Appendix A.5: Convergence at 0.04734 of the p-value between Neck and Lumbar at low frequencies.

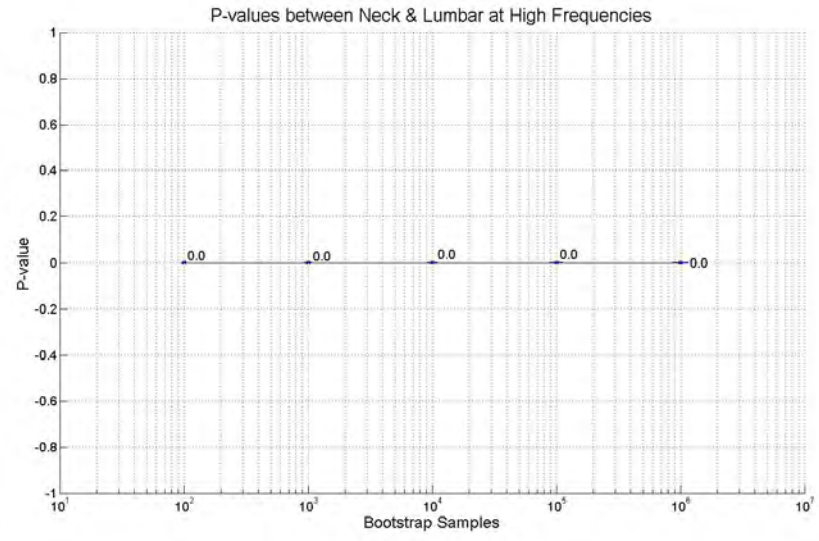

Figure Appendix A.6: Convergence at 0.0 of the p-value between Neck and Lumbar at high frequencies.

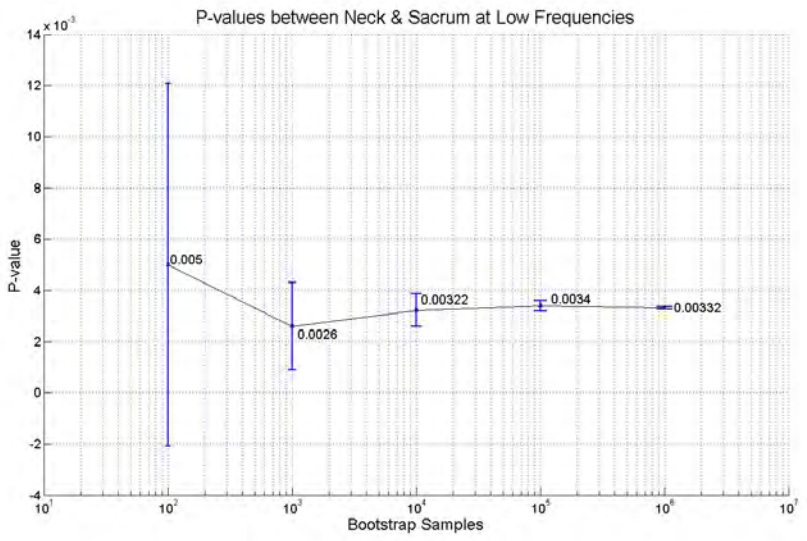

Figure Appendix A.7: Convergence at 0.00332 of the p-value between Neck and Sacrum at low frequencies.

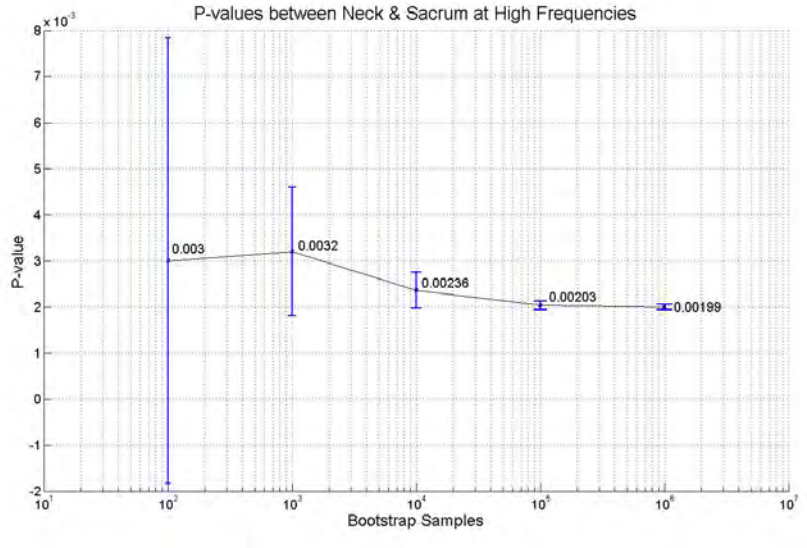

Figure Appendix A.8: Convergence at 0.00199 of the p-value between Neck and Sacrum at high frequencies.

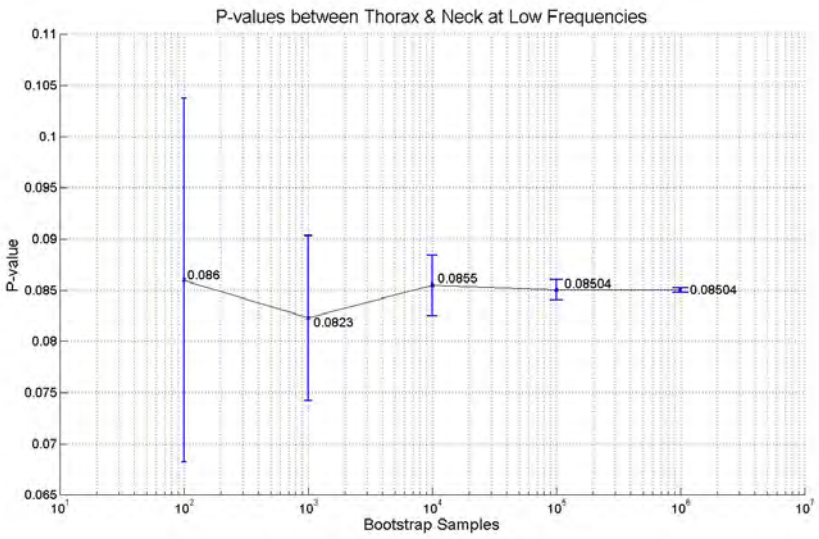

Figure Appendix A.9: Convergence at 0.08504 of the p-value between Thorax and Neck at low frequencies.

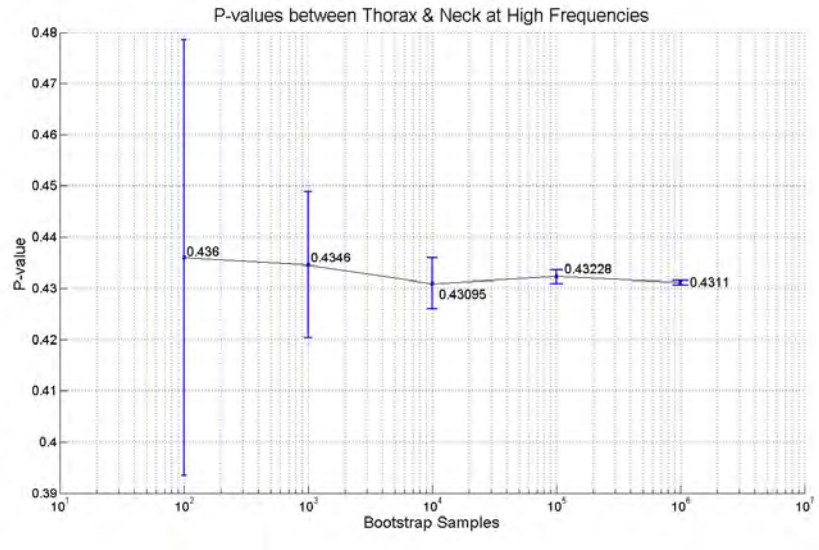

Figure Appendix A.10: Convergence at 0.4311 of the p-value between Thorax and Neck at high frequencies.

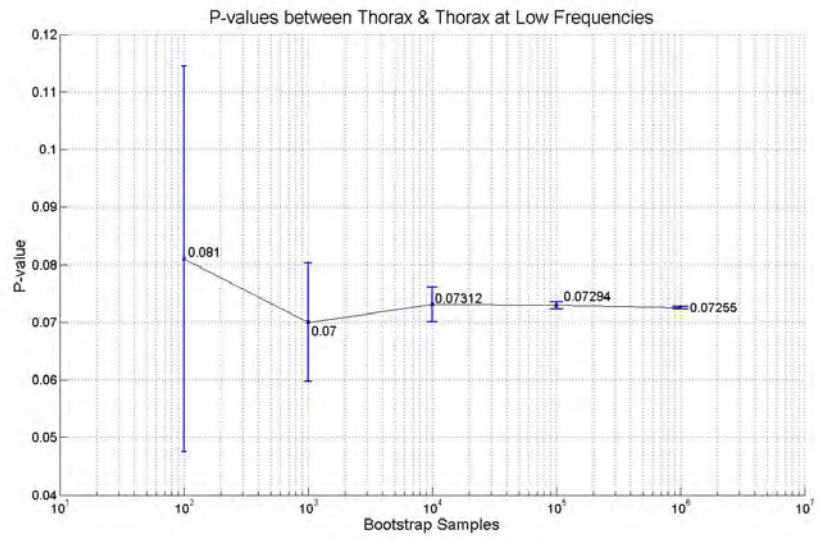

Figure Appendix A.11: Convergence at 0.07255 of the p-value between Thorax and Thorax at low frequencies.

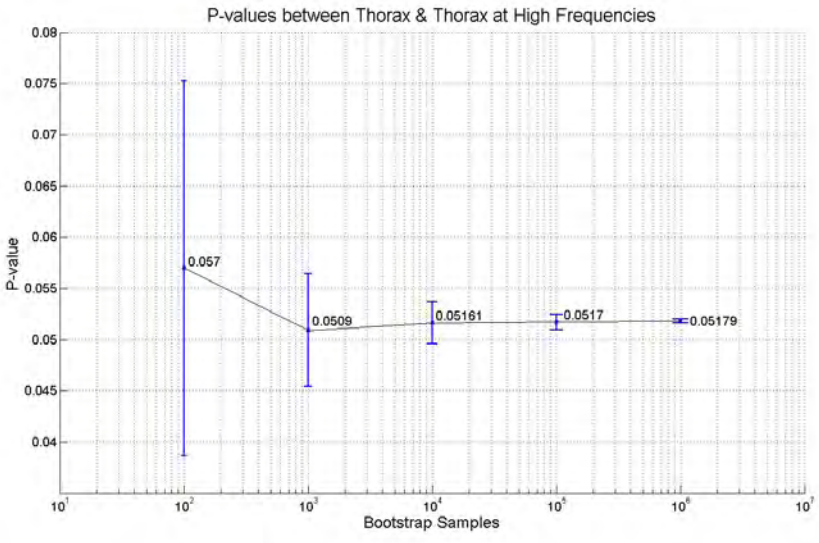

Figure Appendix A.12: Convergence at 0.05179 of the p-value between Thorax and Thorax at high frequencies.

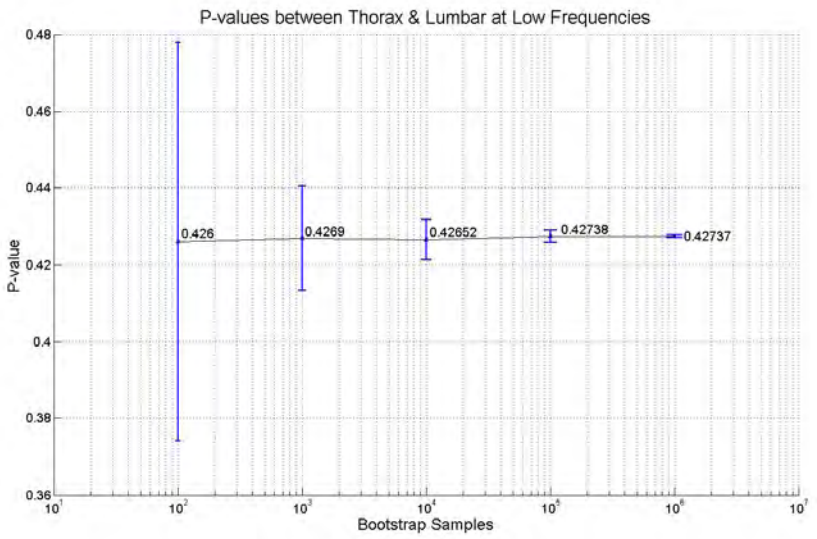

Figure Appendix A.13: Convergence at 0.42737 of the p-value between Thorax and Lumbar at low frequencies.

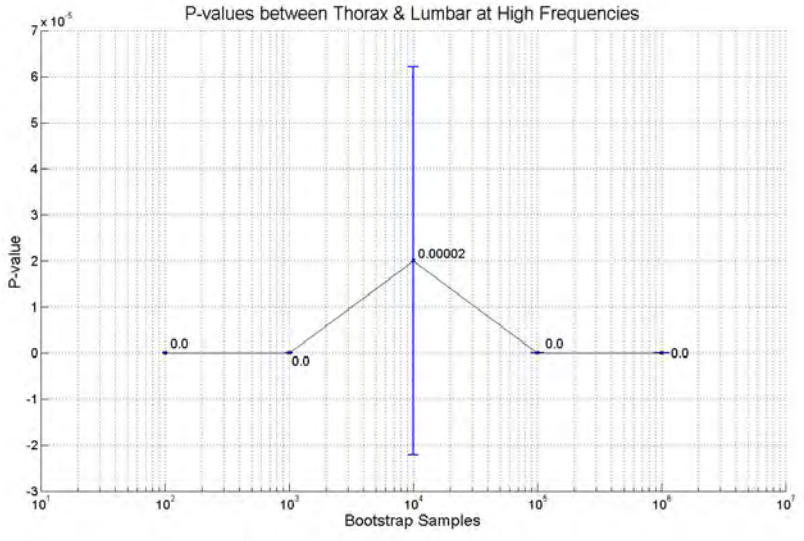

Figure Appendix A.14: Convergence at 0.0 of the p-value between Thorax and Lumbar at high frequencies.

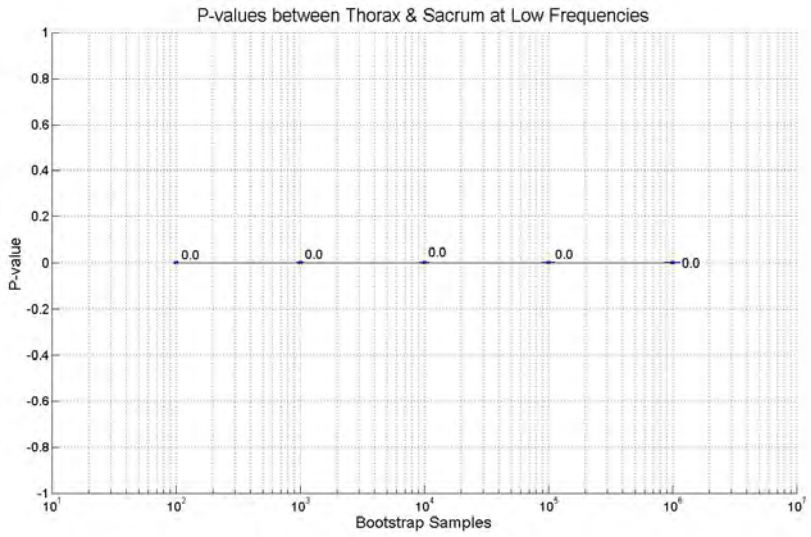

Figure Appendix A.15: Convergence at 0.0 of the p-value between Thorax and Sacrum at low frequencies.

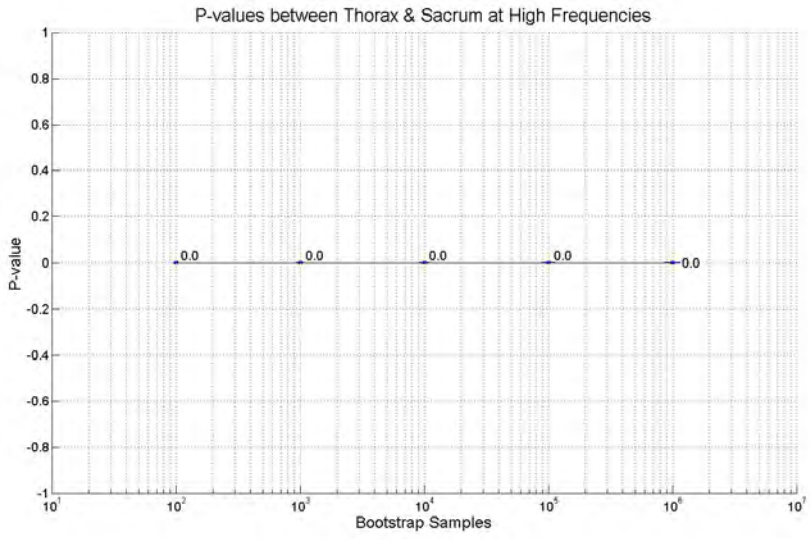

Figure Appendix A.16: Convergence at 0.0 of the p-value between Thorax and Sacrum at high frequencies.

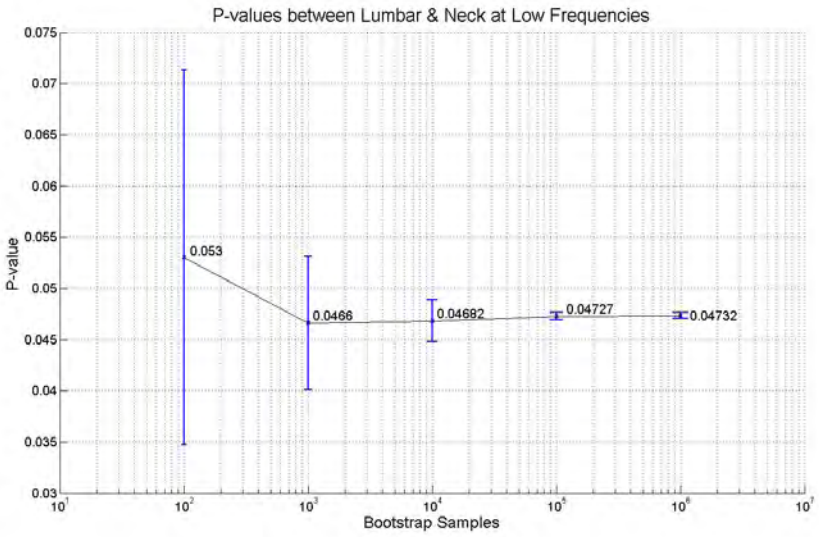

Figure Appendix A.17: Convergence at 0.0732 of the p-value between Lumbar and Neck at low frequencies.

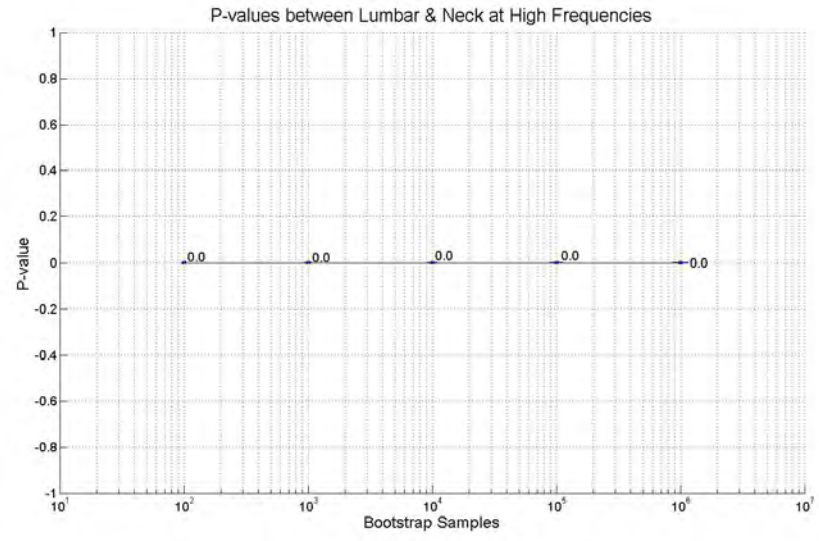

Figure Appendix A.18: Convergence at 0.0 of the p-value between Lumbar and Neck at high frequencies.

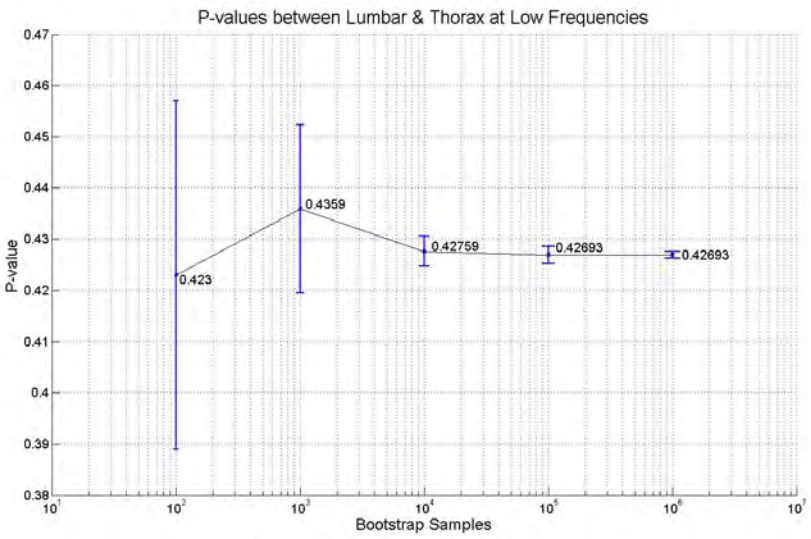

Figure Appendix A.19: Convergence at 0.42693 of the p-value between Lumbar and Thorax at low frequencies.

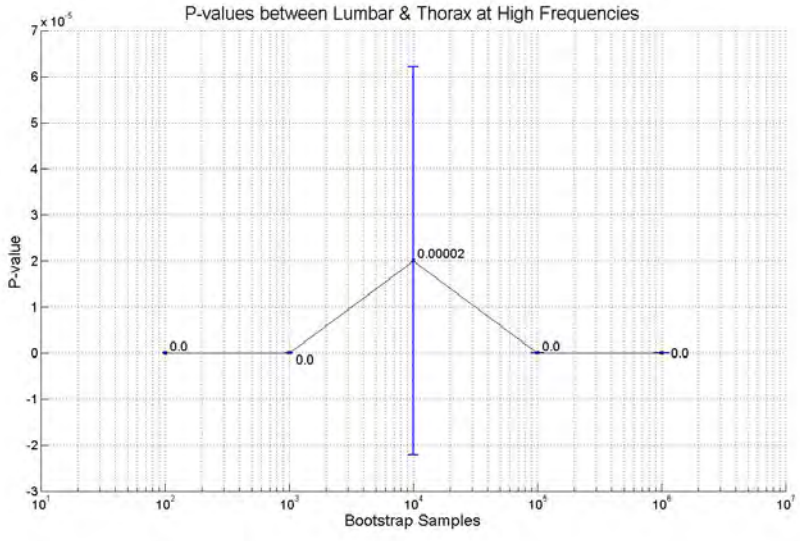

Figure Appendix A.20: Convergence at 0.0 of the p-value between Lumbar and Thorax at high frequencies.

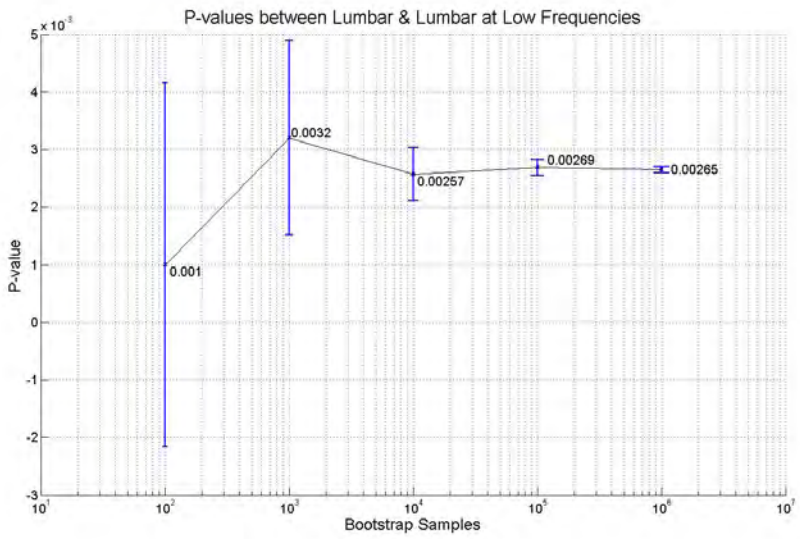

Figure Appendix A.21: Convergence at 0.00265 of the p-value between Lumbar and Lumbar at low frequencies.

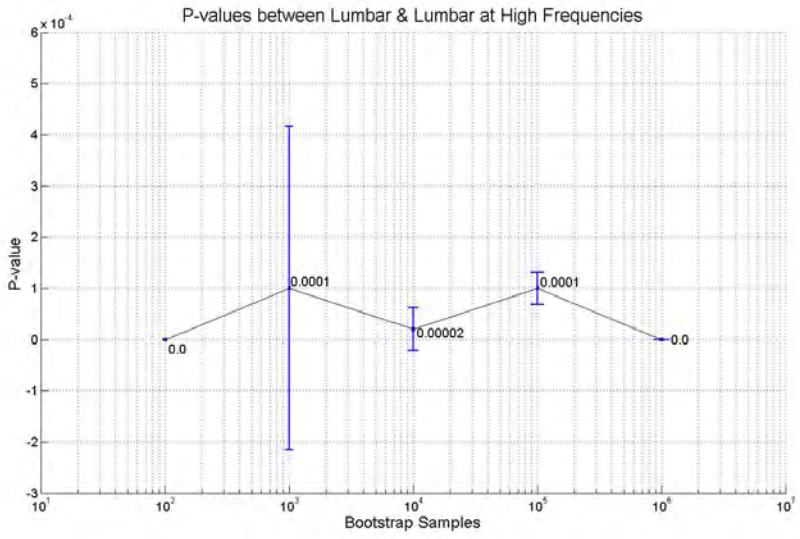

Figure Appendix A.22: Convergence at 0.0 of the p-value between Lumbar and Lumbar at high frequencies.

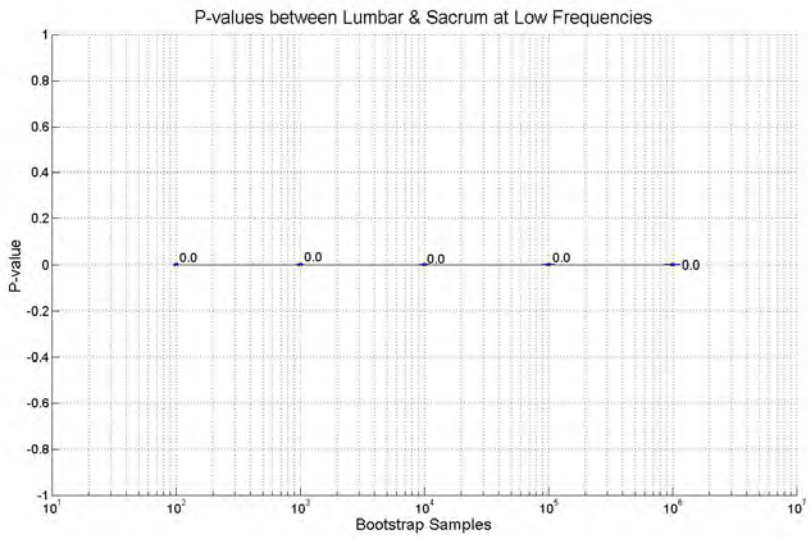

Figure Appendix A.23: Convergence at 0.0 of the p-value between Lumbar and Sacrum at low frequencies.

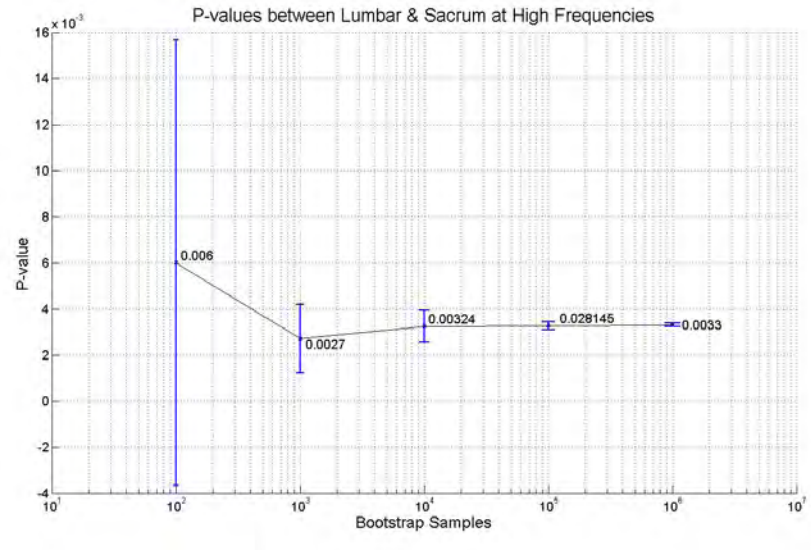

Figure Appendix A.24: Convergence at 0.0033 of the p-value between Lumbar and Sacrum at high frequencies.

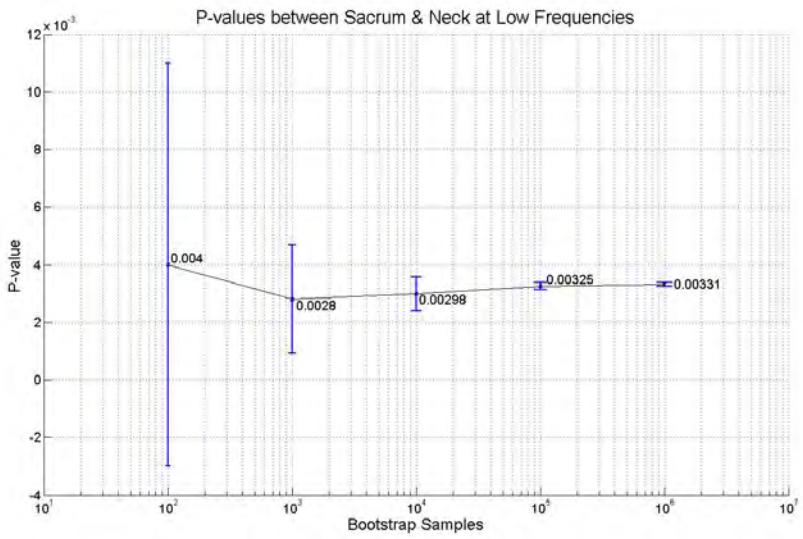

Figure Appendix A.25: Convergence at 0.00331 of the p-value between Sacrum and Neck at low frequencies.

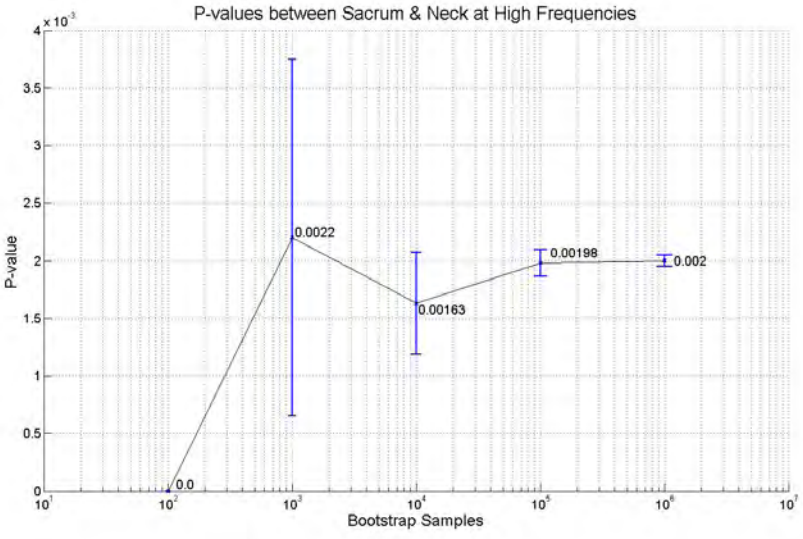

Figure Appendix A.26: Convergence at 0.002 of the p-value between Sacrum and Neck at high frequencies.

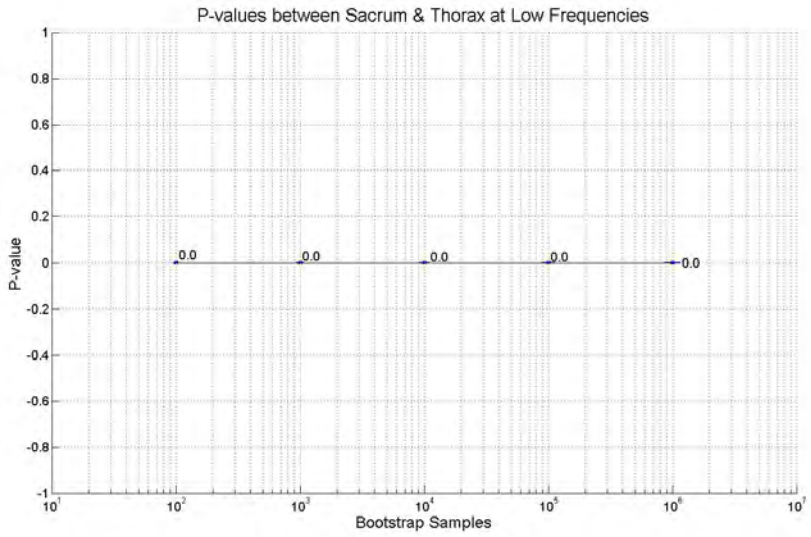

Figure Appendix A.27: Convergence at 0.0 of the p-value between Sacrum and Thorax at low frequencies.

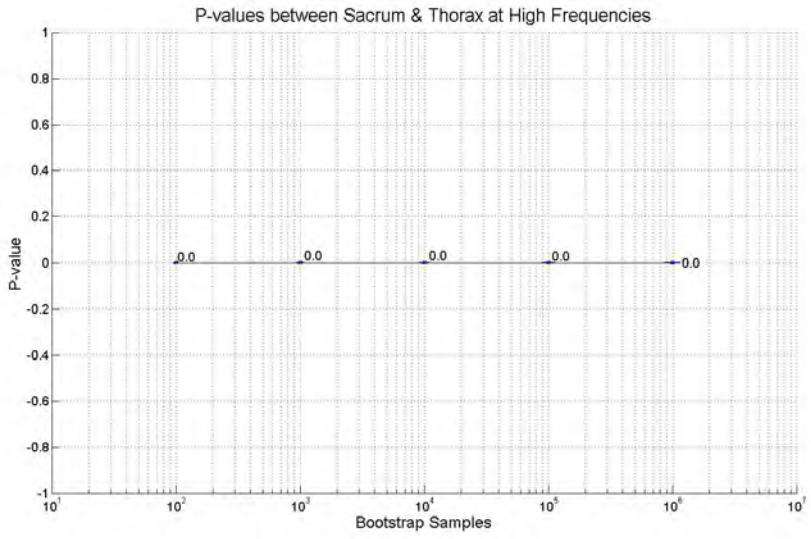

Figure Appendix A.28: Convergence at 0.0 of the p-value between Sacrum and Thorax at high frequencies.

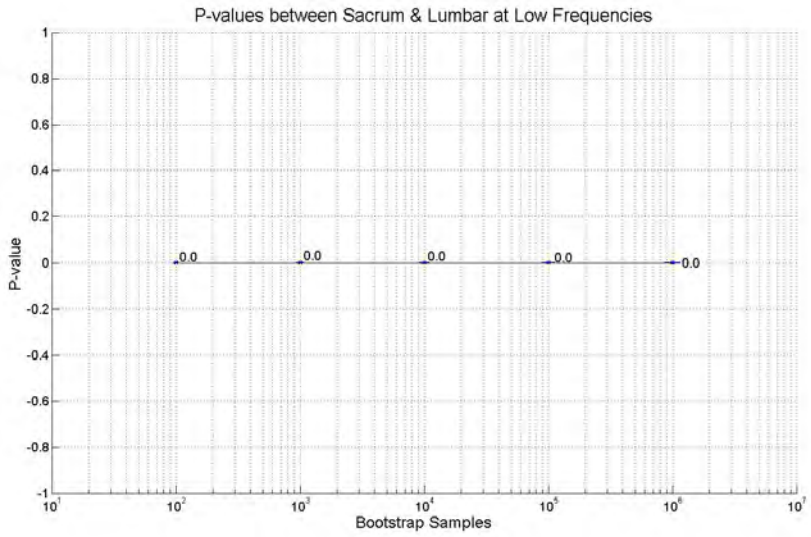

Figure Appendix A.29: Convergence at 0.0 of the p-value between Sacrum and Lumbar at low frequencies.

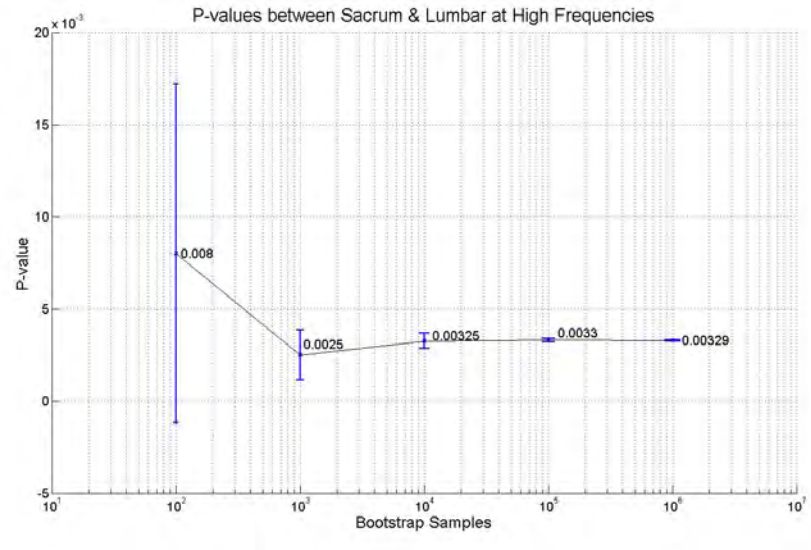

Figure Appendix A.30: Convergence at 0.00329 of the p-value between Sacrum and Lumbar at high frequencies.

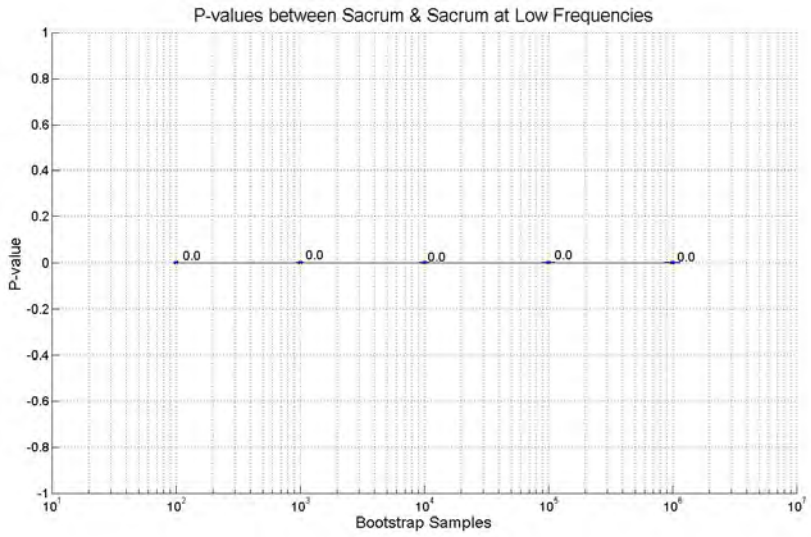

Figure Appendix A.31: Convergence at 0.0 of the p-value between Sacrum and Sacrum at low frequencies.

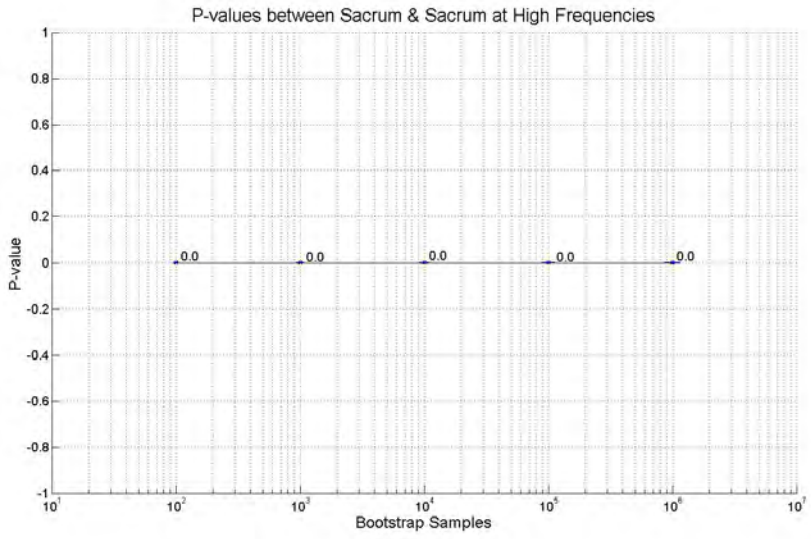

Figure Appendix A.32: Convergence at 0.0 of the p-value between Sacrum and Sacrum at high frequencies.